Department of Materials Science and Engineering

Micromechanical characterization of ALD thin films

Maria Berdova

Aalto University

DOCTORAL
DISSERTATIONS

Aalto University publication series
DOCTORAL DISSERTATIONS 119/2015

Micromechanical characterization of ALD thin films

Maria Berdova

A doctoral dissertation completed for the degree of Doctor of Science (Technology) to be defended, with the permission of the Aalto University School of Chemical Technology, at a public examination held at the lecture hall T2 C105 of Computer Science building, Konemiehentie 2, on October 9th, 2015 at 12.00

Aalto University
School of Chemical Technology
Department of Materials Science and Engineering
Microfabrication group

Supervising professor
Prof. Sami Franssila

Thesis advisors
Prof. Sami Franssila
Prof. Jari Koskinen

Preliminary examiners
Prof. Pasqualina M. Sarro, Delft University of Technology, DIMES, Netherlands
Prof. Victor M. Bright, University of Colorado at Boulder, USA

Opponent
Prof. Weileun Fang, National Tsing Hua University, Taiwan

Aalto University publication series
DOCTORAL DISSERTATIONS 119/2015

ISBN 978-952-60-6344-7 (printed)
ISBN 978-952-60-6345-4 (pdf)
ISSN-L 1799-4934
ISSN 1799-4934 (printed)
ISSN 1799-4942 (pdf)
http://urn.fi/URN:ISBN:978-952-60-6345-4

Unigrafia Oy
Helsinki 2015

Finland

Publication orders (printed book):
aalto.fi

NORDIC ECOLABEL
441 697
Printed matter

Abstract

Aalto University, P.O. Box 11000, FI-00076 Aalto www.aalto.fi

Author
Maria Berdova

Name of the doctoral dissertation
Micromechanical characterization of ALD thin films

Publisher School of Chemical Technology

Unit Materials Science and Engineering

Series Aalto University publication series DOCTORAL DISSERTATIONS 119/2015

Field of research Microelectromechanical systems

Manuscript submitted 31 August 2015 **Date of the defence** 9 October 2015

Permission to publish granted (date) 26 August 2015 **Language** English

☐ **Monograph** ☒ **Article dissertation (summary + original articles)**

Abstract

Atomic layer deposited (ALD) films have become essential for various microelectromechanical systems (MEMS) due to their excellent properties: ALD films are conformal, uniform, dense, and pin-hole free. The main requirement for any film to be applied in MEMS is to exhibit good mechanical properties. Good mechanical properties mean that film has low residual stress, high fracture and interfacial strengths, and known elastic properties under applied mechanical load. MEMS devices are often subjected to the environmental stress. Therefore, it is important to evaluate mechanical properties also after environmental stress conditions. In this doctoral dissertation, the mechanical properties of ALD thin films are evaluated by means of bulge and MEMS shaft-loaded techniques (SLT). Both techniques are very valuable because mechanical properties of thin films are extracted without influence of underlying substrate.

The bulge method is a non-contact method, in which overpressure is applied to load free-standing membrane until it fractures.In the MEMS SLT, the integrated shaft loads free-standing membrane facilitating the extraction of mechanical properties.The developed technique is attractive for characterization mechanical properties of variable thin films due to offered repeatability, precision, and non-piercing nature (the premature fracture by sharp indenter tip is avoided). In this doctoral dissertation, MEMS SLT was employed, in addition, for quantitative and qualitative evaluation of interfacial strength between two thin films.

A new method to study adhesion between extra thin films and various substrates was developed (when conventional scratch testing is not appropriate: when substrates or coatings break before the coating is delaminated). The solution was to embed micro-spheres into the coating. These spheres were laterally detached using microrobotic set-up. This approach facilitated the extraction of interfacial mechanical properties, such as critical load and critical stress needed for removal of a coating.

This doctoral dissertation describes the mechanical properties of ALD Al_2O_3, Al_2O_3/TiO_2 nanolaminates, $Al_xTi_yO_z$ mixed oxide and graphene/ALD Al_2O_3 composites. These materials are promising for MEMS as suspended membranes in thermal devices like bolometers, in chemical sensors like microhotplates and as windows in X-ray optics.

The adhesion properties between sputtered films and ALD Al_2O_3 were measured with MEMS SLT. A new method with the lateral displacement of microspheres led to extraction of interfacial properties between ALD TiO_2 and glass substrate. This information is important to prevent debonding events when fabricating or using MEMS structures.

Keywords Atomic layer deposition, microelectromechanical systems, mechanical properties

ISBN (printed) 978-952-60-6344-7 **ISBN (pdf)** 978-952-60-6345-4

ISSN-L 1799-4934 **ISSN (printed)** 1799-4934 **ISSN (pdf)** 1799-4942

Location of publisher Helsinki **Location of printing** Helsinki **Year** 2015

Pages 119 **urn** http://urn.fi/URN:ISBN:978-952-60-6345-4

Preface

After my master's thesis I got very lucky when I joined Microfabrication group of Prof. Sami Franssila. I am very thankful to Sami not only to a great boss and a leader but also to a great person who inspired me and helped to grow professionally. Every single day I enjoyed working in his group.

I am grateful to a great scientist Kestus Grigoras for his incredible support, help, patience, and positive attitude. He helped me since the beginning to make my first 'test-structures' and continuously was supportive in different kinds of occasions.

I would like to thank all people in MECHALD project. During this project, I learned not only about mechanical properties of ALD thin films, but also how to collaborate and achieve results together. This work was not possible without working with Riikka Puurunen, Oili Ylivaara, Helena Ronkainen, Lauri Kilpi, Xuwein Liu, Saima Ali, Sakari Sintonen, and Timo Sajavaara. Especially I would like to thank for brilliant ideas Prof. Jari Koskinen and Jussi Lyytinen. Together we developed new methods for adhesion characterization.

I wish to thank my colleagues Joonas Heikinen, Sasha Hoshian, Farzin Jahangiri, Li Juan, Giovanni Marin, Ville Jokinen, Anas Al-Azawi, Ashkan Bonabi for cheerful and joyful atmosphere and for the time we spent together. Especially I would like to thank Ville Rontu for the work we made and for his great help.

Big thanks to the research group of Ivan Kassamakov and Prof. Edward Hæggström from the University of Helsinki. It was always the pleasure to collaborate with them.

I would like to thank Jouni Heino and Eija Tuominen, Helsinki Institute of Physics, for the help with pressurizing system for the bulge measurements.

I want to express my gratitude to 'graphene' group: Prof. Harri Lipsanen, Juha Riikonen, Wonjae Kim, Alexander Pyymaki Perros and Li Changfeng. It was great to work with all of them and to achieve new interesting results.

I want to thank the staff of Micronova Nanofabrication Center for running cleanroom and other laboratories in a perfect way.

I would like to thank James Dekker, Feng Gao, Guillaume von Gastrow, Aleksander Kravchenko, Victor Ovchinnikov, Esa Tuovinen, and Leif Grönberg for useful discussions related to cleanroom processing.

Many thanks to Pekka Törmä and Pasi Kostamo from HS Foils for the help to carry out fracture bulge measurements.

I want also to thank the group of Prof. Mika Sillanpää for the work we performed on nanomechanical resonators together.

I am thankful to Prof. Marco Fancuilli for letting me learn more on ALD HfO_2 films during my stay at CNR MDM IMM.

I am grateful for funding and grants provided by Aalto Chemical Technology PhD student grant and by The Finnish National Graduate School in Nanoscience (NGS Nano).

I am grateful to my best friend Galka, who was always so far and so close every time.

I want to thank my mother for her great support and encouragements.

Finally, I am thankful to my small family which made my life meaningful and full of love.

September 2015

Maria Berdova

List of publications

Publication I M. Berdova, T. Ylitalo, I. Kassamakov, J. Heino, P. T. Törmä, L. Kilpi, H. Ronkainen, J. Koskinen, E. Hæggström, and S. Franssila. *Mechanical assessment of suspended ALD thin films by bulge and shaft-loading techniques*, Acta Materialia, **66** (2014) 370.

DOI:10.1016/j.actamat.2013.11.024

Publication II M. Berdova, O. M. E. Ylivaara, V. Rontu, P. T. Törmä, R. L. Puurunen and S. Franssila, *Fracture properties of atomic layer deposited aluminum oxide free-standing membranes,* Journal of Vacuum Science & Technology A **33** (2015) 01A106.

DOI:10.1116/1.4893769

Publication III M. Berdova, A. Perros, W. Kim, J. Riikonen, T. Ylitalo, J. Heino, C. Li, I. Kassamakov, E. Hæggström, H. Lipsanen, and S. Franssila, *Exceptionally Strong and Robust Millimeter-Scale Graphene-Alumina Composite Membranes,* Nanotechnology, **25.35** (2014): 355701.

DOI:10.1088/0957-4484/25/35/355701

Publication IV M. Berdova, J. Lyytinen, K. Grigoras, A. Baby, L. Kilpi, H. Ronkainen, S. Franssila and J. Koskinen, *Characterization of thin film adhesion by MEMS shaft-loading blister testing*, Journal of Vacuum Science & Technology A ***31****(2013) 031102*.

DOI:10.1116/1.4801921

Publication V J. Lyytinen, M. Berdova, S. Franssila and J. Koskinen, *Adhesion Testing of ALD* TiO_2 *on Glass Substrate by the Use of Embedded* SiO_2 *Microspheres,* Journal of Vacuum Science & Technology A **32.1** (2014) 01A102.

DOI:10.1116/1.4827197

Author's contribution

In Publication **I, II, III**, the author designed, developed fabrication process, fabricated the samples, performed bulge and MEMS shaft-loaded tests, analyzed measurement data, interpret results and wrote the manuscript.

In Publication **IV**, the author fabricated and measured the samples, analyzed measurement data, developed methodology of the technique and wrote the manuscript.

In Publication **V**, the author carried out the fabrication process, commented on the manuscript, and made the initial measurements together with the main author.

List of Abbreviations and Symbols

AFM	atomic force microscopy
Al	aluminum
ALD	atomic layer deposition
Al2O3	aluminum oxide
APCVD	atmospheric pressure chemical vapor deposition
Ar	argon
Au	gold
BHF	buffered hydrofluoric acid
Br	bromine
C	carbon
(CF2)n	fluoropolymer
CF4	carbon tetrafluoride
C3F8	octafluoro propane
C4F8	octofluoro cyclobutane
CH4	methane
CHF3	fluoroform
C2H6	ethane
Cl	chlorine
Cr	chromium
CTE	coefficient of thermal expansion
Cu	copper
CVD	chemical vapor deposition
DRIE	deep reactive ion etching
DSP	double side polished
Ea	activation energy
EDX	energy dispersive X-ray microanalysis
H2	hydrogen
H2O	water
HF	hydrofluoric acid
HMDS	hexamethyl disilazane vapor
KOH	potassium hydroxide
LPCVD	low-pressure chemical vapor deposition
MEMS	microelectromechanical systems
NbN	niobium nitride
NEMS	nanoelectromechanical systems
NH3	ammonia

O2	oxygen
O3	ozone
PECVD	plasma enhanced chemical vapor deposition
PMMA	polymethyl methacrylate
RF	radio frequency
RIE	reactive ion etching
SEM	scanning electron microscopy
SF6	sulfur hexafluoride
Si	silicon
SiC	silicon carbide
SiH4	silane
SiO2	silicon dioxide
SiOxFiy	silicon oxyfluoride
Si3N4	silicon nitride
SLBT	shaft-loaded blister testing
SLT	shaft-loaded testing
SWLI	scanning white light interferometry
Ti	titanium
TiCl4	titanium chloride
TiO2	titanium dioxide
Tm	melting temperature
TiN	titanium nitride
Ts	substrate temperature
TMA	trimethylaluminum
TMAH	tetramethyl ammonium hydroxide
TOF-ERDA	time-of-flight elastic recoil detection analysis
UHCVD	ultrahigh vacuum chemical vapor deposition
UV	ultraviolet
XRR	X-ray reflectivity

Contents

Preface 4
List of publications 6
Author's contribution 7
1. Introduction 11
2. Thin film deposition techniques 16
  2.1. Physical methods 16
  2.2. Chemical methods 20
3. Thin film physical and chemical characterization 27
4. MEMS materials and fabrication 30
  4.1. Microfabrication technologies 30
5. Characterization of residual stress, elastic modulus and fracture strength 48
  5.1. MEMS devices as tools for thin film mechanical characterization 48
  5.2. Young's modulus, residual stress and fracture strength of ALD Al_2O_3, mixed oxide $Al_xTi_yO_z$ and nanolaminated Al_2O_3/TiO_2 thin films ... 55
6. Adhesion 58
  6. 1. Definition of adhesion 58
  6. 2. Methods for determination of adhesion 59
7. Summary and conclusions 68
Appendix 71
  1. Weibull analysis 71
References 74

1. Introduction

Microdevices contain many different thin films. Device reliability is greatly influenced by the mechanical properties of these films. A functional failure of a single structure can degrade or even destroy performance of the entire component. Therefore, it is essential to understand the mechanical properties of thin films, and to develop techniques and procedures for evaluating their mechanical performance.

Thin films are fundamental structural materials in microelectromechanical systems (MEMS). In particular, there are many MEMS devices with free-standing structures and movable elements, which carry different mechanical loads. Suspended membranes perform as critical elements in micropumps, microhotplates, X-ray windows and other devices [1,2]. In micropumps suspended membranes deliver some fluid per each pump cycle [1,3,4]. Microhotplates consist of heater and sensing films located on free-standing membrane for minimal power dissipation [5,6]. In X-ray windows ultra-thin membranes transmit X-ray photons and absorb unwanted radiation [7,8]. For instance, low-pressure chemical vapor deposited (CVD) silicon nitride membranes films can transmit more than 50% of soft X-rays (50–250 eV).

Thinnest films are only one atomic layer thick. The continuity of films strongly depends on material and deposition method. For example, Al_2O_3 with the thickness of less than 1 nm is continuous when deposited by atomic layer deposition (ALD) [9], whereas evaporated Au film is continuous only when thickness exceeds 5 nm [10]. As the thickness increases the residual stresses can reach excessive levels, limiting film thicknesses typically to a few micrometers [11,12].

Thin films are two dimensional systems with properties that are different from the bulk. For example, thermal conductivity of polysilicon thin films is an order of magnitude lower than that of bulk silicon, and unlike bulk silicon it increases with increasing of temperature. Electron mobility is likewise an order of magnitude smaller, while Young's modulus is similar. Coefficients of thermal expansion (CTE) are comparable: 2.7 ppm/°C and 3.07 ppm/°C, respectively, for both polysilicon thin film and single crystal silicon [13,14].

Mechanical properties of thin films include Young's modulus and residual stress. Young's modulus (E) is a measure of elastic response to the applied stress.

It is determined from the linear part of the stress-strain (σ-ε) slope of a material following Hooke's law:

$$\sigma = E^{'}\varepsilon + \sigma_0, \qquad (1)$$

where (σ_o) is residual stress, E' is the biaxial modulus, defined as $E/(1-\nu)$. The strain is described as dimensionless quantity of relative material elongation: $\varepsilon = (l' - l_0)/l_0$ (l' is final length under stress and l_o is the original length). Stress is defined as the ratio of the force F to the area over which F is applied. Young's modulus and residual stress can be extracted from load-deflection measurements (Publication **I**, Publication **II**, Publication **III**).

Independent of deposition technique films are always in a state of stress. Residual stress is a measure of disorder between substrate and thin film introduced during thin film deposition (intrinsic stress) and/or thermal treatment (thermal stress). The intrinsic stress is related to film microstructure and it develops during the film growth. Thermal stress develops when film and substrate with undergo thermal treatment at a temperature higher or lower than film deposition temperature. Typically film and substrate have CTE, and they contract or expand differently as a function of temperature. Therefore during a temperature change both materials are constrained, resulting in thermal stress. When the thermal expansion coefficient of the film is larger than of the substrate, then during the temperature ramp down the substrate shrinks less than film and restricts the film from shrinking, therefore tensile stress results. In contrast, if the thermal expansion coefficient of the film is lower than of the substrate, then the substrate shrinks more than the film during cooling from elevated to room temperature, therefore compressive stress results (Figure 1).

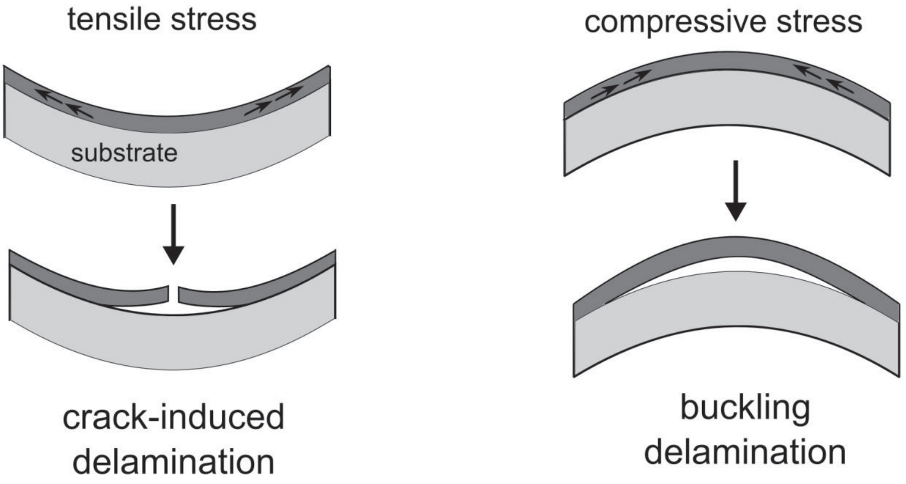

Figure 1. Thin film failure under high residual tensile or compressive stress.

Thin films can undergo adhesion failure due to excessive residual stress. If the thin film is under high residual stress, then cracking-delamination events can take place. In the case of high tensile stress, coating undergoes crack induced delamination (Figure 1), whereas under excessive compressive stress buckling/blistering can occur (buckling driven delamination) as a relief of stored energy. The buckling can continue and form patterns called “telephone cords”: sinusoidal motion in the film plane [15].

Uncontrollable residual stress degrades device performance causing bowing and deformation of substrate, film cracking or delamination. Furthermore, the stress can influence optical or magnetic properties [16]. In micromirrors, it is desired that free-standing structures are ideally flat to provide stable reflecting properties. Therefore, the residual stress of structural films should be low enough. Typically, in magnetic MEMS, very thick electrodeposited films are used. Often residual stress increases with thickness resulting in cracking, deformation of devices, and interfacial failure.

Device mechanical performance can be improved by multilayered structures. To improve adhesion, an adhesive layer of, e.g., 10 nm of Ti or Cr is often grown. This layer promotes bond formation between different layers. Multilayers can be also used to compensate excessive residual stress. The combination of films with compressive and tensile stresses can be used to reduce total stress of a multilayer structure, as shown for Al_2O_3/NbN/Al_2O_3 in Figure 2. This approach was used in our work [17] to minimize compressive stress and therefore improve electromechanical performance of NbN resonator with 50 nm Al_2O_3 and TiO_2 layers deposited by ALD. Due to the nature of ALD, the films were grown on both sides simultaneously, assuring symmetrical stress compensation. As deposited sputtered NbN beams exhibited high compressive residual stress of – 2.2 GPa and high bending. The formation of multilayered structure with symmetrical layers of 50 nm ALD Al_2O_3 reduced the stress to 973±25 MPa, and to 772±28 with 50 nm TiO_2, resulting in flat released beams.

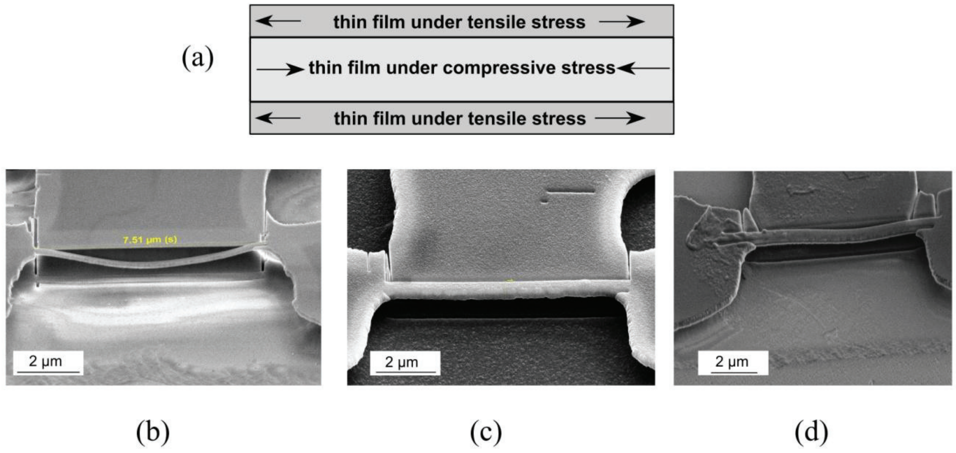

Figure 2. (a) Schematic image of multilayered stress compensation mechanism, (b) Scanning electron microscope (SEM) image of NbN NEMS without ALD (residual stress of – 2.2 GPa), (c) SEM image of multilayered NEMS with TiO_2 (residual stress of 772 MPa), (d) SEM image of multilayered NEMS with Al_2O_3 (residual stress of 973 MPa) [17].

Nanolaminates consist of periodically alternating layers of two or more materials with the layer thicknesses in the nanometer range. As a result of periodic stacking of different layers, the nanolaminated structures exhibit particular composite physical properties. The resulting properties can be tailored by tuning thickness of each laminate layer. It opens new possibilities for a great number of applications. For example, ultra-low thermal conductivity (<1 W/mK) can be reached with W/Al_2O_3 nanolaminates [18]. These nanolaminates have high interface density and large phonon frequency difference between each layer so that phonons are scattered at the interface, reducing thermal conductivity. Different deposition methods can be used to compose nanolaminated structures. Evaporation and sputtering are supplied with shutters able to turn deposition off. To achieve a perfect nanolaminated structure a layer-by-layer growth is preferred. ALD provides ideal nanolaminates with sharp interfaces. Each ALD layer forms continuously and uniformly. The accurate thickness control during ALD growth is beneficial when growing nanolaminated structures, particularly when each layer is very thin.

There are numerous techniques for measuring mechanical properties of thin films. Nanoindentation and wafer curvature methods are routinely used to characterize Young’s modulus and residual stress. However, the utilization of these techniques and further data interpretation are limited by a number of factors. Nanoindentation suffers from substrate effects and pile-up of the material around indenter [19]. These are especially problematic for very thin films, like the ALD films studied in this thesis. Wafer curvature relies on theoretical model which relates the residual stress of the film to change in substrate radius of curvature after film deposition. In case of poor adhesion between the substrate and film, or if film is very thin and non-uniform the technique suffers from scatter in the data [16]. Novel accurate methods are, therefore, required to obtain reproducible, reliable data to overcome these limitations. The interpretation of data obtained from suspended (free-standing) films is less ambiguous because influence of the underlying substrate and any adhesion issues between film/substrate are minimized, or eliminated.

The goal of the thesis

The purpose of this thesis was to investigate the mechanical properties of thin films used for MEMS applications. Among them there are atomic layer deposited (ALD) films (Publications **I**, Publication **II**, Publication **III**). In Publication **I**, mechanical properties of suspended ALD thin films, such as Al_2O_3, mixed oxide ($Al_xTi_yO_z$) and nanolaminates (Al_2O_3/TiO_2) were studied by two approaches: bulge and MEMS shaft-loaded methods. In Publication **II** fracture properties of free-standing ALD Al_2O_3 thin films were obtained by means of a bulge test. Fracture strength was investigated as a function of deposition temperature, and after thermal (annealing) and environmental (humidity) stress. Publication **III** concentrates on a method for improving the mechanical robustness and stability of suspended Al_2O_3 film by incorporating a graphene monolayer. In Publication **IV** novel method for quantitative and qualitative assessing of adhesion energies and critical adhesion stress between two thin films (ALD Al_2O_3 and sputtered Pt, Cu, Cr/Cu) was developed and evaluated by MEMS shaft-loaded technique. The critical adhesion stress between ALD TiO_2 and glass substrate is studied by a new method, where SiO_2

spheres are embedded into the coating and afterwards detached by mechanical lateral load (Publication **V**).

Structure of the thesis

The thesis includes a brief overview of deposition techniques, the microstructure of resulting films and residual stress (Chapter **2**). Chapter **3** contains description of physical and chemical methods used for films characterization. Chapter **4** is dedicated to MEMS fabrication technologies. Lithography, wet and dry etching and annealing methods are described. In Chapter **5**, methods to evaluate fracture, residual stress and Young's modulus are discussed and compared in detail. Chapter **6** describes the basics of adhesion, and methods used to determine adhesion. Finally, summary and conclusions are given in Chapter **7**. The work presented in this thesis hopefully finds use in thin film and MEMS communities, and helps in introducing new materials, deposition processes, and microdevices.

2. Thin film deposition techniques

Many thin film deposition techniques exist, resulting in flexibility in choosing materials and tailoring their properties. Thin films can be grown by various chemical and physical deposition methods. If the material deposited is a product of chemical reaction, the process is classified as chemical. Chemical methods include CVD and ALD. Physical methods, e.g., evaporation, sputtering, refer to those deposition techniques when a source material is ejected from the source and the film is formed by condensation of atom vapor. The resulting film microstructure can be crystalline, amorphous or polycrystalline depending on chosen deposition technique and deposition conditions.

2.1. Physical methods

1) Eva*poratio*n

In evaporation, the source material is located in water-cooled crucible and then evaporated through heating. Heating is commonly performed by electron beam (Figure 3). Consequently atoms of the source materials are ejected, and thin film is formed from the condensation of vapor of heated material. Thin films with a high purity can be evaporated from a high purity source material made from any solid shapes. Typically evaporation rates are in the range of 0.1–10 nm/s [12]. High vacuum is required to avoid collisions of atoms.

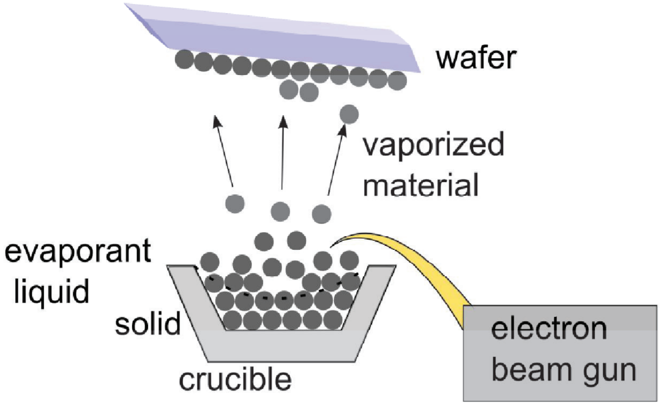

Figure 3. Basic principle of evaporation: electron beam heats source material, vapor is transported towards substrate forming a film.

Microstructure

In a simple model, the microstucture of evaporated films is defined by normalized substrate temperature to the melting temperature of the target: Ts/Tm (in K) [20,21]. Three main zones of different microstructures can be distinguished (Figure 4). The low temperature zone *I*, Ts/Tm <0.3, contains small columnar weakly binding grains with porous morphology. Zone *II* develops at higher temperatures, 0.3<Ts/Tm<0.5, with straight columnar grains with higher binding energies and, therefore, smoother and denser structure due to higher mobility of adatoms to find energetically favorable places. Zone *III* (Ts/Tm>0.5) consists of large crystalline structure due to increase in the diffusion into the grains and elimination of voids [22,23].

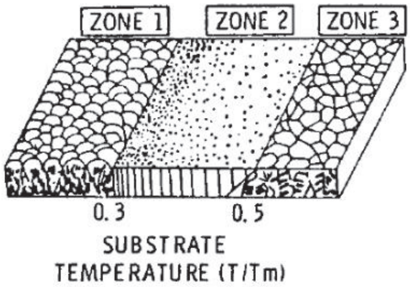

Figure 4. Structure-zone model. The microstructure of a pure elemental film depends on the ratio of deposition temperature to the melting temperature, taken from [21].

Residual stress

Typically evaporated thin films experience excessive residual stress, therefore, their utilization is limited [24]. Moreover, substrate type, aging time, and film thickness influence the stress [25,26]. Majority of evaporated films have tensile stress, which can be up to 3 GPa. However, materials with a high affinity for oxygen (Al, Ti, SiO_2) or with a lot of impurities can also be under compression [25-28]. In the zone *I*, tensile stress manifests when microstructure consists of weakly binding grains separated by voids. Tensile stress changes to compressive with the densification of a film (zone *II*, zone *III*). Evaporated materials with low melting points, e.g., Ag (1234 K), Cu (1356 K) or Al (933 K) exhibit both tensile and compressive stress. However, high melting point materials, e.g., Fe (1808 K) or Zr (1855 K), are usually in the state of tensile stress (zone *I*).

2) Sputtering

Sputtered films form by ejecting target materials by ion bombardment (Figure 5). Accelerated by high voltage, gas ions (typically Ar^+) impinge the target surface biased negatively. As a result, ejected atoms or molecules are transferred in vacuum to a substrate forming a coating by condensation of sputtered species.

Modern sputtering systems use magnetrons. Magnetic field lines trap electrons in the plasma; hence electrons circulate around the target without dissipation on chamber walls. This incorporated magnetic field increases ionizing electron-atom collisions and therefore the number of bombarding ions [29]. This leads to depositions of relatively dense films with high deposition rates up to 1 μm/min.

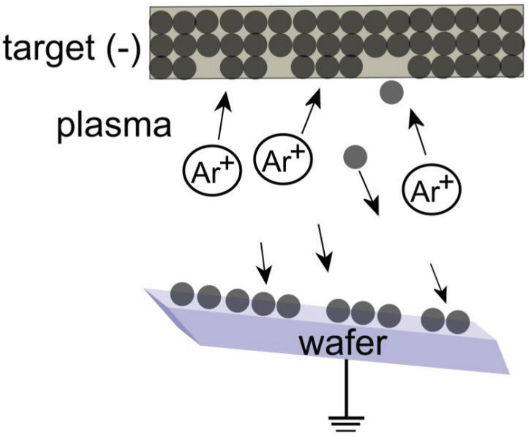

Figure 5. Basic principle of sputter deposition: target atoms are ejected by Ar^+ ions and then transferred towards the substrate forming a film by condensation.

If oxygen or nitrogen is added to the sputtering along with argon, then oxides and nitrides will form by means of chemical reaction of the target material and the introduced gas (reactive sputtering).

Microstructure

The same simple T_s/T_m model can be applied to the crystallinity of sputtered films [21,30]. The neighboring crystallites enlarge with increasing temperature until no space remains between them. Amorphous films form at low temperatures and at high deposition rates. Low temperature reduces the diffusion of adatoms to seek for equilibrium lattice sites [31]. This leads to porous films (zone *I*). Relatively high substrate temperatures yield to high mobility of atoms and as a result to dense and close-packed microstructures (zone *II*) [27]. In the zone *III*, films (typically deposited at high substrate temperatures or containing a lot of impurities) consist of globular grains with random orientations [31]. Zone *T* refers to a transition zone that is unique when ion assistance is present ($T_s/T_m < 0.3$). The transition zone *T* between zone *I* and zone *II* is defined as a region when sputtered deposition is performed at reduced gas pressures. Zone *I* can be additionally subdivided into three zones: *Ia*, *Ib*, and *Ic* [31]. At very low temperatures, thin films of the zone *Ia* and *Ib* are amorphous because adatoms have only little mobility, whereas thin films of the zone *Ic* are polycrystalline due to increased mobility with temperature. The microstructure can be additionally influenced by bombardment energy, thin film thickness, and gas flows. This allows forming various thin films with various structural, mechanical or electrical properties [32-34].

Residual stress

The stress-zone correlation can be applied for sputtered films. However, this model, in addition to process temperature, takes into account process pressure levels. When the microstructure is porous (zone *I*), the stress is tensile (Figure 6). In this region, thin film is unable to maintain high stress due to high porosity. With the conversion to zone *T*, the tensile stress reaches its maximum as voids collapse. Afterwards, microstructure becomes fully compact and dense (zone *II*), and the stress changes sharply to compression [27]. The gas pressure influences the transport behavior of sputtered atoms, microstructure, and therefore residual stress level. If gas pressure is low, there are fewer collisions with the ambient gas. Then more energy can be supplied the surface, which results in denser films that are typically in compression (zone *II*). At high working pressures, sputtered atoms have less energy and, therefore, columnar microstructure with voids form and tensile stress dominates (zone *I*) [29,33,35].

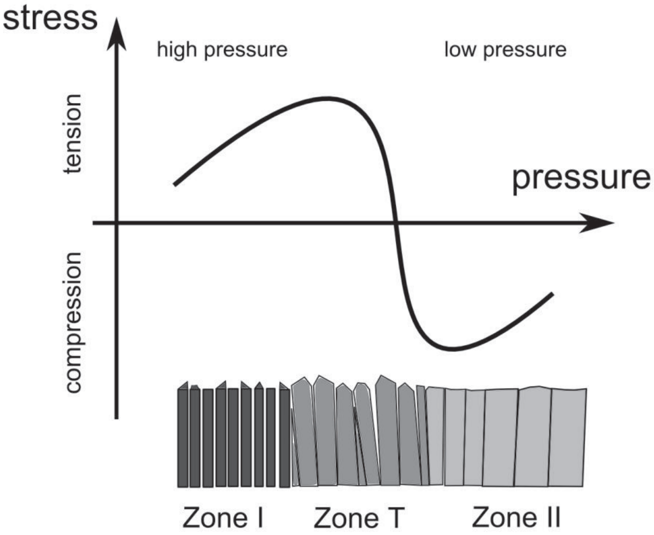

Figure 6. Stress-zone correlation (adapted from [26]).

Due to complexity of plasma process, the intrinsic stress of sputtered films depends also on other parameters. For example, the stress of sputtered chromium has the maximum tensile stress of ~750 MPa with zero bias voltage. It becomes compressive after ~50 V bias voltage following saturation of – 1 GPa after 75 V bias voltage [35,36]. The mechanical properties of reactive sputtered NbN undergo changes depending on deposition conditions. NbN widely used in superconductive applications, where high transition temperatures are needed. One can achieve very high transition temperature (12–15 K) and high compressive residual stress (-2.2 GPa) at the same time [17,37,38]. Increasing of sputtering current increases stress, but decreases transition temperature, and therefore reduces the applicability of the material.

In some cases the substrate type, deposition rates, crystal orientation can additionally influence mechanical properties [33,39].

2.2. Chemical methods

1) Chemical vapor deposition

Chemical methods refer to those when a new material is grown by means of surface chemical reactions [12,39,40]. Chemical vapor deposited (CVD) layers are composed by bringing vapor phase precursors to a substrate (Figure 7). The reaction at the surface results in a solid layer of material. The coating formation involves a number of key steps: [12,40-42]

1. Transport of gaseous reactive species into reaction chamber.
2. Diffusion of gaseous species to the substrate.
3. Adsorption of reactants onto the heated substrate.
4. Diffusion of reactants on the substrate surface.
5. Chemical reaction at the surface leading to film formation.
6. Gaseous by-products are diffused out.
7. Unreacted source gas molecules and volatile by-products are transported away from reaction chamber.

CVD methods vary according to activation or enhancing of the reaction mechanism. The activation can involve thermal energy (thermal CVD), plasma (plasma-enhanced CVD), or light (photo CVD). Depositions using photo CVD may occur even at room temperatures since decomposition of the gases occurs through photochemical reactions. In this method, however, the deposition rate is very slow and it limits its widespread applications [41]. Thermal CVD requires high temperatures, 500–1400°C. Plasma CVD can work at lower temperatures, i.e. 300–500°C. The lower deposition temperatures are beneficial for fabricating devices consisting of temperature sensitive materials. Furthermore, at low temperatures residual stress is reduced due to smaller thermal mismatch between substrate and film.

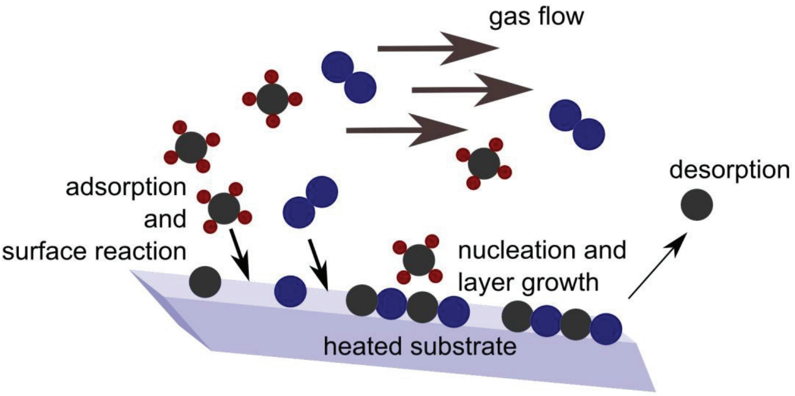

Figure 7. Basic principle of CVD: coating is formed by chemical reaction on a substrate (adapted from [12]).

Thermal CVD is subdivided based on pressure range at which the deposition takes place:

- atmospheric pressure (APCVD): 760 Torr
- low pressure CVD (LPCVD): ~1 Torr
- ultrahigh vacuum CVD (UHVCVD): less than 10^{-5} Torr.

LPCVD yields dense films with very uniform thickness and better conformality than APCVD. Atmospheric pressure reactors, however, are cheaper and simpler. Reduction of impurities and better control of the deposition is achievable by UHVCVD. Impurities like hydrogen, can be reduced by sufficiently low process pressure.

The deposition rates typically are in the range from 0.1 to 10 nm/s [12] and follow Arrhenius law increasing exponentially with deposition temperature:

$$Rate = z(t)\exp\left(-\frac{E_a}{kT}\right), \qquad (2)$$

where E_a is the activation energy (eV), $z(t)$ is a constant, T is deposition temperature (K), k is the Boltzmann constant. Activation energy is defined as a slope from the plot of deposition rates in logarithmic scale versus reciprocal deposition temperatures. Activation energies differ depending on CVD method. For example, LPCVD Si_3N_4 from silane SiH_4 and ammonia NH_3 has activation energy of 1.1 eV. In PECVD process plasma activates reactive species. Therefore PECVD Si_3N_4 has lower activation energies ranging from 0.11eV to 0.31eV [43,44].

When the process temperatures are low and high flow rates supply the surface with enough reactants, then the process is surface reaction limited. In this regime, when the temperature increases, the deposition rates exponentially increase following Arrhenius law. But when the process temperatures are high, then all gas sources react at the surface. Then the deposition rate depends on the gas supply (mass transport limited process). Mass transport limited process can suffer from the local depletion of the reactants because fast surface reactions consume all of gas supply. Thus surface reaction limited process result in more uniform films than the mass transport limited reactions [12].

Microstructure

Many parameters influence the microstructure of CVD films. Gas ratios, types of precursors, process temperatures determine the grain size and surface roughness [45,46]. The film thickness often defines the microstructure of CVD films: the thicker the film, the larger the grain size. As the film becomes thicker, columnar grains start to develop [42].

The relation of process temperature and microstructure has similar general trend as materials deposited by physical methods. Therefore, it becomes possible to control the CVD microstructure by proper manipulation of the deposition conditions. The increase in temperature leads to higher surface mobility of the species, and hence to larger and closely packed grains. The diffusion is minimized at low pressures, therefore fine-grained structure results. The same fine grains are obtained at low temperature and high concentration of reactive species. Amorphous films grow at even lower temperatures and at higher concentrations of the reactants.

Residual stress

In general, the mechanical properties of CVD films are very sensitive to process conditions [47,48]. For instance, tailoring gas flows (NH_3/SiH_4) and deposition temperature of PECVD Si_3N_4 leads to various stress levels from 400 MPa, tensile, to – 600 MPa, compressive [47]. Impurities can influence the residual stress level. The stress of PECVD Si_3N_4 increases from compressive of – 600 MPa at 300°C to tensile 600 MPa at 700°C as a function of decreasing hydrogen in the film with increasing temperature [49]. LPCVD Si_3N_4 films exhibit high tensile stress of 950 MPa at deposition temperature of 725°C. The increase of deposition temperature decreases the tensile stress to 700 MPa at 775°C [43]. The difference in the stress level of LPCVD and PECVD Si_3N_4 is mainly due to different hydrogen content in the films. Relatively large amount of hydrogen (up to 30%) is present at low temperatures when deposited with PECVD process, whereas deposited at high temperatures LPCVD Si_3N_4 films are stoichiometric with very low hydrogen content. As a consequence, low-temperature PECVD Si_3N_4 has lower densities, higher etch rates, and poor stability in humid environment since films absorb large amount of water.

Graphene CVD synthesis

CVD technique can be used for synthesis of a single layer of carbon atoms arranged in two-dimensional manner: graphene [50,51]. The graphene synthesis typically involves polycrystalline nickel or copper substrate, which is exposed to carbon-based gas at high temperatures. As the substrate cools down, carbon precipitates on the surface to form graphene. Copper is preferred because it provides smoother and more uniform graphene monolayer whereas nickel yields to graphene flake formation [52]. The difference is associated with the growth mechanism: on Ni graphene forms by diffusion from the substrate and on Cu it forms by catalytic decomposition on the surface with ultralow solubility into the Cu. The process stops when the copper layer is fully covered by carbon atoms (self-limiting growth).

To facilitate graphene transfer to any other target substrate, polymethyl methacrylate (PMMA) is applied onto graphene by spin-coating. Then underlying copper is chemically etched to detach a graphene monolayer with PMMA for the further transfer. Subsequently, PMMA is dissolved in acetone, leaving only graphene on a target substrate [51,52].

Graphene has great electrical and optical properties: it has high electrical conductivity and it is able to absorb 2.3% of visible light [53]. The light transmittance reduces with increasing of graphene layers. These properties can be utilized to build, for example, transparent electrodes for optical detectors and photovoltaics. Graphene distinguishes from other materials also by its high mechanical properties: 1TPa of Young's modulus, and high fracture strength of 130 GPa [54]. The incorporation of a single monolayer can significantly improve mechanical performance of various polymers [54,55] and ceramics

(Publication **III**). In particular, the introduction of graphene increases the mechanical strength and crack tolerance.

2) Atomic layer deposition

Atomic layer deposition (ALD) is a chemical method. ALD relies on cyclic surface reaction of precursors with a solid surface [56-58]. In one ALD cycle two compounds are sequentially injected into the chamber with a purge (typically nitrogen) in-between to remove unreacted precursors and reaction products (Figure 8). In the simplest model, one ALD cycle consist of the following steps:

1. Pulse of the first precursor on a sample surface; first half reaction.
2. Purge to remove unreacted precursors and reaction products.
3. Pulse of the second precursor on a sample surface; second half reaction.
4. Purge to remove unreacted precursors and reaction products.

As a result of each cycle, supplied material is grown on a sample surface within one ALD cycle (growth per cycle). Each surface reaction continues until all available reaction sites are covered (self-terminating growth) and the ALD process proceeds in a layer-by-layer fashion until desired amount of material is deposited. This facilitates formation of a thin conformal layer of a material even on complex, nanoporous, high aspect ratio structures and large-area substrates [59,60].

The deposition temperatures of ALD films are relatively low. For example, Al_2O_3 can be grown even at 33°C with a growth per cycle of 1Å/cycle and very low roughness of 4±1Å [61]. The possibility of using low temperatures makes this technique attractive for growing different layers on thermally sensitive substrates and structures.

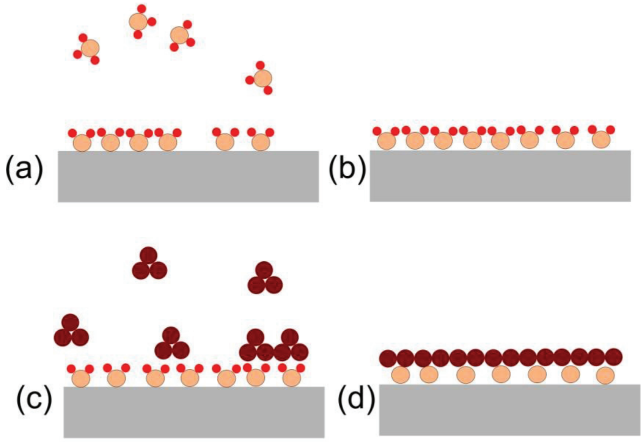

Figure 8. Basic ALD principle: (a) saturation of the first precursor on a sample surface (b) reaction products and unreacted precursors are purged away (c) reaction of the second precursor with the first layer (d) reaction products and unreacted precursors are purged away.

ALD process involves pulses of two volatile precursors separately from each other, whereas in CVD process all gases are supplied simultaneously and continuously. The separation of precursors leads to self-terminating growth of uniform film, whereas simultaneous process may result to non-uniform film thickness due to fast surface reactions. Another ALD benefit is the elimination of gas-phase reaction. The precursors are injected separately one by one with the purge in-between. The purge helps to avoid gas-phase reaction. Simultaneous process can also suffer from poor conformality when deposited on substrates with high aspect ratios: precursors can deplete in deep structures. As a result, more material grows on the top than on the bottom of the feature.

Each ALD reaction occurs within the certain temperature range, typically within 80–500°C, called ALD-window. In this range, the ALD reactions continue in a self-terminating mode [57]. Outside the range excessively high temperatures promote gas-phase reaction in CVD-like fashion or to partial decomposition of the precursors [62]. Low temperatures lead to precursor condensation or to significant reduction of the deposition rate [63].

Many ALD reactions remain, however, mildly temperature dependent within the ALD-window. One example is aluminum oxide, the most studied ALD material. It is deposited usually with trimethylaluminum ($AlMe_3$, TMA) and water (H_2O) or ozone (O_3) as precursors. The growth of Al_2O_3 follows the reactions:

$$2Al(CH_3)_3 + 3H_2O \rightarrow Al_2O_3 + 6CH_4 \qquad (3)$$

$$2Al(CH_3)_3 + O_3 \rightarrow Al_2O_3 + 3C_2H_6. \qquad (4)$$

In the first half cycle, TMA reacts with OH-terminated surface with hydrogen, forming volatile methane groups and leaving aluminum bonded to oxygen. Next, in the second half cycle, the water or oxygen reacts with CH_3 groups, forming more volatile species and leaving OH-terminated surface [56,64]:

$$AlOH^* + Al(CH_3\ )_3 \rightarrow Al - O - Al(CH_3\ )_2^* + CH_4^g \qquad (5)$$

$$AlCH_3^* + H_2O\ \rightarrow AlOH^* + CH_4^g \qquad (6)$$

$$AlCH_3^* + O_3\ \rightarrow AlCH_2OH^* + C_2H_4^g \qquad (7)$$

The ALD window for TMA and H_2O process is 30°C to 300°C. Higher temperatures lead to decomposition of TMA and to deposition of aluminum, which is further oxidized by H_2O to form CVD-like Al_2O_3 layer [65]. The deposition rates (growth per cycle) are typically in the range of 0.9–1.2 Å/cycles depending on deposition temperature within ALD window. The deposition rate of Al_2O_3 is known to decrease linearly with deposition temperature. The dependence is opposite to expected typical CVD deposition rate which is exponentially temperature dependent according to Arrhenius law. The decreasing trend of ALD Al_2O_3 growth per cycle is determined by the decrease of surface species, i.e. AlOH and $AlCH_3$, at higher temperatures [56].

Titanium dioxide from titanium tetrachloride ($TiCl_4$) and H_2O is another common ALD reaction [66]:

$$TiCl_4 + 2H_2O \rightarrow TiO_2 + 4HCl \qquad (8)$$

or two half reactions

$$TiOH^* + TiCl_4 \rightarrow Ti - O - TiCl_3^* + HCl^g \qquad (9)$$

$$TiCl^{*} + H_2O \rightarrow Ti(OH)^{*} + HCl^{g} \qquad (10)$$

where * and ^{g} indicate surface and gaseous species.

The typical ALD window for this process is 80–600°C. The deposition decreases with the increasing temperature saturating above 200°C. The growth per cycle decreases from 0.65Å/cycle at 80°C to 0.53Å/cycle after 200°C. The saturation is probably related to the change in crystallinity [67,68].

Microstructure

ALD films start to grow in amorphous or crystalline form. Temperature, film thickness, substrates, impurities, reactants influence the microstructure of inorganic ALD films. The microstructure changes with process temperature. High mobility of the species at higher temperatures promotes grain formation. For example, as deposition temperature of Al_2O_3 increases films become denser. However, only annealing can change their amorphous form to crystalline [69,70]. Interesting example is TiO_2, which starts growing as an amorphous film, but after a certain thickness crystalline columnar grains start to form [71]. In some cases the impurities determine the microstructure. For example, high amounts of carbon impurities in TiN films prevent crystallization. Large grains form with low carbon concentrations independently of deposition temperature [70].

Residual stress

Mechanical properties of only some ALD thin films have been studied: mainly of Al_2O_3 and TiO_2 on planar substrates. Typically ALD films exhibit residual tensile stress in the range of hundreds MPa. The stress decreases with higher deposition temperature for Al_2O_3 [69], but increases with higher deposition temperature for TiO_2 [67].

Nanolaminates and multilayers using ALD

ALD is capable of growing conformal nanolaminated structures with highly precise periodicity and thickness [56,72]. The nanolaminates can improve corrosion resistance or gas diffusion, tune refractive index, and vary resistivity depending on nanolaminate system [70,72-74].

This thesis focuses on nanolaminate system: ALD Al_2O_3–ALD TiO_2 (Publication **II**). Our nanolaminates Al_2O_3/TiO_2 consisted of 4 nm bilayer with individual 2 nm thick layers (50% volume fraction). Al_2O_3 layers were grown with trimethylaluminum (TMA) and water process, and TiO_2 with titanium chloride and water at 220°C. The targeted 2 nm individual layers were achieved by 48 cycles of titanium dioxide (0.425Å/cycle), and by 19 cycles of aluminum oxide (1.1 Å/cycle).

Composite ALD Al_2O_3-CVD graphene (Publication **III**) consisted of two layers of ALD aluminum oxide (70 nm and 30 nm) separated by a single graphene layer. Deposition of aluminum oxide was done with trimethylaluminum and water precursors. The graphene layer was seeded with evaporated aluminum which was further oxidized in air to Al_2O_3 to facilitate further ALD Al_2O_3 growth on graphene.

3. Thin film physical and chemical characterization

Characterization of thin films is necessary for further thin films utilization and optimization of their deposition processes. Thin film microstructure, roughness, thickness can be characterized using optical or probe techniques. During optical characterization, thin films interact with incident beam light and reflected beam is used to obtain film characteristics. In the probe measurements, a stylus scans the sample to extract surface properties.

Optical methods, including ellipsometry and reflectometry, are capable of measuring thin film thickness with sub-nm scale precision (can be used to measure optical constants, too). Often whole wafer is scanned to obtain statistical data about thickness uniformity. Ellipsometry is based on measurement of change in polarization when light is reflected [12]. Optical reflectometry of the thickness consists of comparing the path lengths of the light reflected from the film and from the substrate. Reflectometry is based on measuring the amount of the reflected light from the sample surface over a range of wavelengths.

Scanning Electron Microscopy (SEM) is an important technique for three-dimensional characterization of surface features. It consists of focused high-energy electron beam (5-100keV), which scans line by line the surface of a sample to form an image by means of interaction between the beam and the sample. The response is transmitted by collecting reflected electrons (backscattered) or secondary electrons (released from the atoms) with following converting of the response to electrical signal and it's amplifying to produce a contrast image [75].

Many SEMs are equipped with *Energy dispersive X-ray microanalysis (EDX)* to identify and quantify chemical composition. EDX is based on detection of characteristic X-rays emitted from a sample during electron irradiation. The emitted X-rays are detected by a detector to generate a spectrum of X-ray intensity versus X-ray energy. Elemental analysis is performed by the examination of characteristic peaks of spectra. Therefore, the analysis yields the elemental composition of the film at the specimen surface, ca. 1 µm.

Film thickness, density and roughness can be measured by means of *X-ray reflectivity (XRR)*. The method relies on measuring the intensity of reflected X-rays from the sample when the reflected angle is equal to the incident. The reflectivity changes depending on film structural parameters. Therefore, the X-ray reflectivity curves are correlated with the thickness, density and roughness of the thin film by fitting the simulation curve to the experimental spectra. X-ray reflectivity is suitable for determination the interfacial roughness between individual layers of nanolaminated structures and/or for observation intermixing of individual layers (intermixed structures has no superlattice maximum) [76].

Atomic force microscopy (AFM) measures topography (feature dimensions) and morphology (shape and texture). AFM consists of a sharp probe mounted at the end of a cantilever. During the measurement, sharp probe scans in the *x,y*-directions over the surface and cantilever deflection (in *x,y,z*-directions) is measured as a function of scanning force to provide high-resolution lateral and vertical image. Film roughness and grain sizes are identified as a result of distance-dependent interaction forces between the probe and sample surface. Probe techniques are also used to scan a step formed after etching to measure the thickness.

Scanning white light interferometry gives information about thickness, surface quality, and feature dimensions. The technique can also provide fast and accurate imaging of deflections of MEMS suspended structures with nm-scale *z*-resolution (Publication **I**, Publication **III**). The method is based on interference phenomenon of two (or more) beams of light [33]. In the SWLI, two beams are created by splitting the main beam from white light source. One beam is then reflected by the reference mirror (reference beam), whereas another beam scans the sample surface. The reflected light from the surface recombines with the reference beam creating bright and dark lines (interference pattern or fringes). Each interferogam represents the variation in the intensity as a function of scan position. The 3D and 2D surface images are obtained by fitting of the interferograms to the envelope function. The maximum of the envelope function is then correlated with the relative surface position [77].

Ion beams are very useful for determination compositional and structural properties of various films. After the impact of high-energy ions with the sample, the backscattered ions are collected to characterize material properties. In *time-of-flight elastic recoil detection analysis (TOF-ERDA)*, sample surface is bombarded with a beam of accelerated ions, e.g., Cl and Br (>200keV). In this technique, the velocity and energy of sample atoms, which are recoiled in forward direction by the incident heavy ion, are measured in coincidence (Figure 9). These energy-time-of-flight histograms can be converted to form depth profile of elements as masses. Using TOF-ERDA it is therefore possible to determine stoichiometry and impurities such as carbon, hydrogen, nitrogen [78].

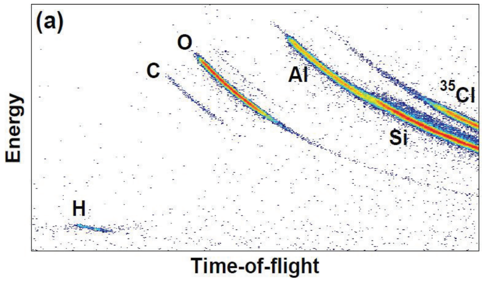

Figure 9. Elemental analysis using TOF-ERDA: the time-of-flight–energy histogram from as deposited 100-nm-thick Al_2O_3 sample grown with TMA and O_3 precursors.

4. MEMS materials and fabrication

MEMS device performance and life-time depend on materials properties. Due to the fact that MEMS consist of moving structures, it is necessary that materials exhibit predictable and reproducible properties under mechanical deformation [79]. Reliable device performance depends on reproducible fabrication process with a high yield. Lithography, dry and wet etching, various thin film deposition techniques, wafer bonding make it possible to fabricate complex but robust structures.

4.1. Microfabrication technologies

1) Surface pretreatment

Surface preparation is an easy, but very important step in microfabrication. For instance, unpredictable delamination of a film can occur during film deposition in case of presence of contaminations, e.g., if some photoresist is left after lithography. Contaminations can prevent etching of some areas, acting as local etch masks.

Wet cleaning is the main method to clean the sample surface. Typically, cleaning of silicon substrates is performed in hydrogen-peroxide-based (RCA) wet cleans. Two main solutions, i.e. RCA-1 (H_2O_2-NH_4OH-H_2O) and RCA-2 (H_2O_2-NCl-H_2O) are used to remove contaminants. The RCA-1 removes particles, organic contaminants and some metals, whereas RCA-2 removes alkali metal hydroxides and heavy metals.

The photoresist residues can be removed in acetone and isopropyl alcohol. Oxygen plasma or acetone ultrasonic cleaning can be performed in case if polymer residues are still on the sample surface. Sulfuric acid and hydrogen peroxide mixture (piranha) remains, however, the most common and powerful cleaning technique to remove organic residues. However, it is dangerous and relatively difficult to handle. Annealing in oxygen atmosphere at 1000°C is an alternative way to remove organic residues [12].

If thin films is deposited over native oxide, then the device performance, e. g., electrical, can degrade because native oxide is rough and non-uniform. Removal of native oxide is done using hydrofluoric acid (HF). This treatment results in hydrophobic silicon surface, which repels water and does not react significantly with oxygen. In addition, some metals like aluminum can be removed with HF. Alternatively, oxide layer remaining on the wafer surface can be desorbed by the thermal treatment, for example in H_2 ambient, at temperature 800°C and higher.

Wet cleaning is followed with rinsing and drying. Therefore, it is crucial that these processes are done properly to avoid recontamination of wafers. Rinsing is performed in high purity DI-water. It helps to remove any weakly bound species from the surface, for example, fluorine species after HF cleaning. Vapor drying, lamp drying, spinning, or nitrogen blowing finish the cleaning cycle.

Changing surface chemistry may result in the formation of a necessary chemical bond. For example, often pretreatments of the silicon are performed to facilitate uniform oxide formation on the surface. For example, prior the ALD deposition ozone pre-exposure showed promising results for electrical applications: the dielectric constant significantly increased after ozone pretreatment [80].

2) Lithography

Lithography is a method to transfer a pattern onto the wafer. Usually, when pattern is to be etched, lithography is employed to define the etch mask. Prebake, which removes adsorbed water, is followed by hexamethyl disilazane vapor (HMDS, $(H_3C)_3$–Si–NH–Si–$(CH_3)_3$) treatment. HMDS acts as an adhesion promoter between photoresist and substrate. It also prevents water adsorption from ambient. After the spin-coating of a resist onto a substrate and prebaking, the wafer is exposed by the UV-light to change chemical solubility of the resist in a developer. Developer is a liquid solution which clears the exposed parts or unexposed parts depending on the resist. The resist is called positive when exposed areas are dissolved by the developer, and conversely, it is called negative when exposed areas remain insoluble. Hard bake is commonly utilized after the exposure to solidify the resist, to drive-out any remaining solvents, to improve adhesion, and to minimize residual photoactive components. After further processing (e.g., etching) photoresist is stripped using acetone or oxygen plasma. Then processing continues.

Lithographical methods are classified according the source of light: UV-radiation, electron, and laser beam sources (Figure 10). In the optical lithography, ultra-violet light source exposes the wafer with photoresist through the mask. Modern mask-aligners uses argon fluoride excimer lasers with the wavelength of 193 nm to achieve smaller linewidths. Masks are typically made of quartz with chromium patterns, which block the light. In the e-beam lithography, focused electron beam scans the area to form a pattern. E-beam lithography enables better resolution and eliminates the mask. Laser direct writing is also a maskless method where laser beam scans the resist to create a feature of interest. The laser beam (typically light source of 405 nm and 375 nm) pulses with adjustable pulse lengths and different spot sizes (to define the pattern resolution). The pattern is produced by moving either the stage with the sample or the laser beam above the certain fixed sample area [81,82].

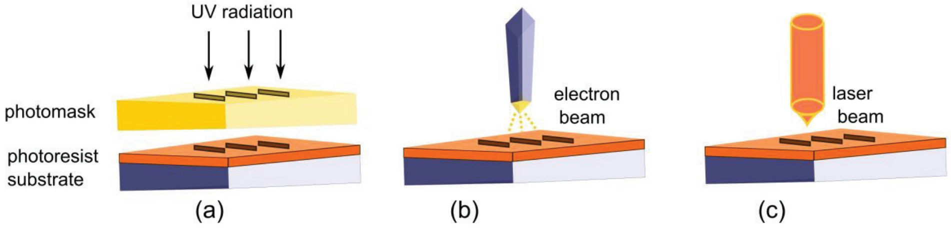

Figure 10. (a) Optical; (b) electron beam; (c) laser lithography.

Often it is necessary to fabricate structures containing multiple layers. Therefore the alignment of each layer with respect to other layers must be accomplished. The first pattern includes a set of alignment marks at defined places. These marks are further used to position subsequent patterns (masks). Figure 11 shows a multilayered structure of membrane resonator fabricated using e-beam lithography and lift-off process [83].

The first pattern (Figure 11) is a bonding pad and a gate electrode, whereas the second pattern is used to support free-standing membrane [83]. The membrane resonator (third pattern) is micromanipulated onto supports (second pattern) using a sharp glass needle and actuated by gate electrode (first pattern). Since the supports and gate electrode has different thickness, therefore the alignment of the first pattern to the second is required. The process flow for the resonator is

1. Fabrication of the gate electrode with alignment marks (first pattern)
    - Electron - beam lithography
    - Evaporation of 50 nm of aluminum
    - Lift-off in acetone.
2. Fabrication of support structure where the aluminum membrane is placed on (second pattern)
    - Electron - beam lithography
    - Evaporation of 200 – 250 nm of aluminum
    - Lift-off in acetone.
3. Membrane fabrication and micromanipulation (third pattern)
    - Electron - beam lithography
    - Evaporation of 50 nm of aluminum
    - Lift-off in acetone
    - Catching the separated thin metal film (aluminum membrane) by copper loop and locating onto the support structure.

As can be seen from the Figure 11, the first and second patterns are very close to each other; and any possible misalignment between them can cause failure of the designed structure.

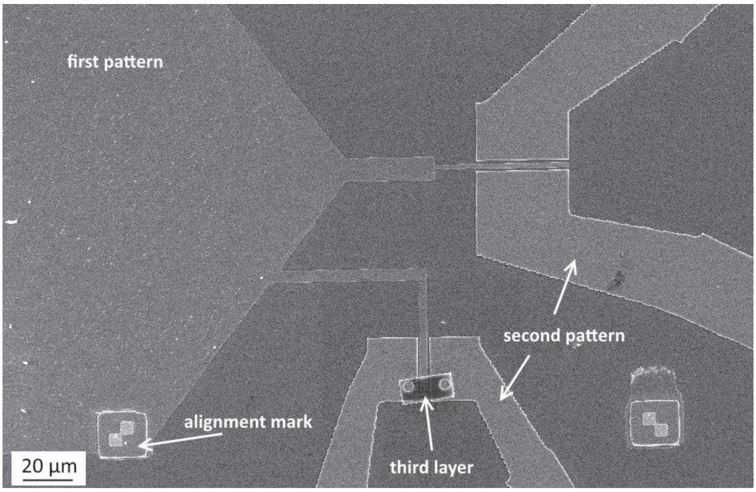

Figure 11. SEM image of multilayered structure [83].

3) Wet etching

A great advantage of wet etching is simplicity; therefore it is widely used in microfabrication. In wet etching, the substrate is immersed into wet etchant to etch exposed areas. Amorphous materials are etched always isotropically, i.e. homogeneously in all directions. However, some etchants etch crystalline materials depending on crystal orientation (anisotropically). For instance, potassium hydroxide (KOH) and tetramethylammonium hydroxide (TMAH) etch the (100) and (111) silicon crystal planes selectively since different planes have different bond densities exposed to the etchant [12]. The selectivity between (100) and (111) planes is 200:1 and 30:1 in KOH and TMAH, respectively. The utilization of high quality etch mask is crucial during TMAH or KOH etching. Thermal silicon dioxide, LPCVD silicon nitride or heavily doped boron silicon are commonly used for this purpose.

Etching of silicon dioxide and aluminum oxide is performed in HF. HF-based etchants are also often used to remove native oxide. During wet oxide etch, photoresist and silicon nitride serve as etch masks. The etch rates for different oxides vary with the etching temperatures. The etch-process temperature increases etch rates significantly. For instance, for ALD Al_2O_3 it rises from 40 nm/min at room temperature to 114 nm/min at 32°C in buffered HF (BHF). Therefore, to maintain stable etching it is necessary to keep the temperature constant.

Wet etching for free-standing structures

The fabrication of free-standing structures often involves wet etch release using bulk or surface micromachining (Figure 12).

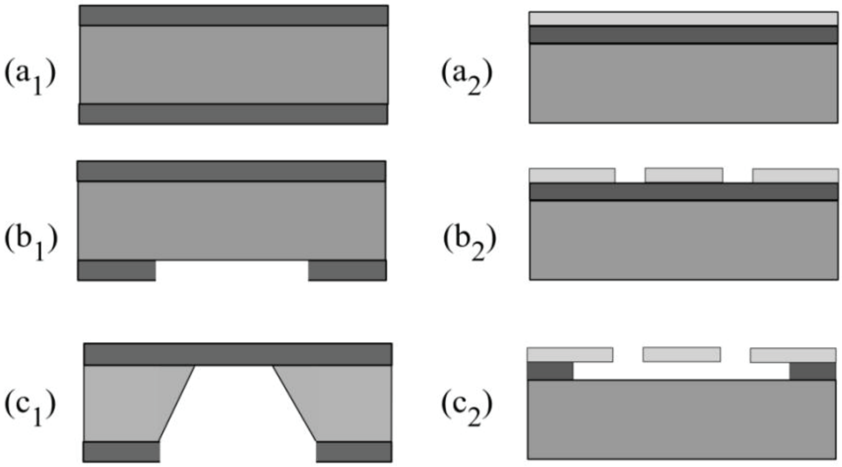

Figure 12. Fabrication of free-standing structures: (a$_{1\text{-}2}$) deposition of thin film; (b$_{1\text{-}2}$) patterning to define geometry of free-standing structures; (c$_{1\text{-}2}$) wet etch release of the wafer or sacrificial layer.

In the bulk micromachining (Figure 12 (a$_1$-c$_1$)), wet etching of silicon is used. This method is fast and easy to implement, however, membranes only of rectangular shapes can be fabricated due to fast etching of (100) and slow etching of (111) crystal planes. Surface micromachining (Figure 12 (a$_2$-c$_2$)) is based on selective removal a layer underneath of the structural layer. For example, if the sacrificial layer is oxide, then HF-based etching is employed to release the structure. However, the method is challenging due surface tension issues appearing during the drying step.

It is desired that the structural released layer has low residual stress. If the stress is highly tensile the functional layer can undergo cracking, whereas high compressive stress leads to the bulking of the released layer (Figure 13). However, low tensile stress is desired to ensure flatness of released structures.

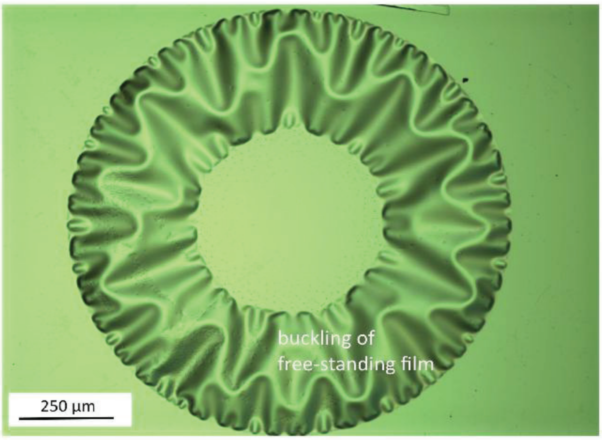

Figure 13. Buckling of suspended sputtered Pt membrane due to compressive stress.

Thin films on the top of structural layer, e.g., electrodes, can be deposited before and after the etch release. The deposition is preferred on finished free-standing structures, i.e. after etch release, especially when using noble metals, like gold and platinum (Publication **IV**). Contamination of the process lines is, as a result, avoided. This method is also useful when ready-made membranes are required or in case if further deposited materials can be etched during the etch release. However, in this approach, membranes are prone to damage if fabrication involves further processing. Spin-coating, lift-off, high temperature treatments can destroy membranes due to induced thermal stress or surface tension related problems. When thin films are deposited before membrane release, no process-induced damage occurs. But thin films have to be compatible with the process conditions. This method was used in the Publication **III**: graphene transfer was done prior dry etch release to avoid any possible membrane damage. The alternative method of deposition of thin films on free-standing structures is the combination of both approaches. It starts from partial release, then continues with metallization and finishes with final release of free-standing structure. It provides more mechanical stability of released structure, shorter final release, and, thereby, higher fabrication yield.

4) Reactive ion etching (RIE)

Reactive ion etching is a key process for majority of MEMS devices. One can easily obtain various high-aspect ratio (width:depth ratio), anisotropic or isotropic structures using plasma-assisted dry etch. In RIE, ionized gas forms chemically active and ionic species via dissociation and ionization processes. For example, SF_6 gas is ionized to create ionic F^- and SF_x^+ and chemically active F^* species. Chemically active species react with the material, break chemical bonds and, as a result, form volatile products (chemical etch). Ion species enhance the etch rate by bombarding the surface (physical etch) [12,84,85]. Oxide and nitride etching is typically done with CHF_3, C_2F_6, C_3F_8 or C_4F_8 plasmas [86]. Silicon is typically etched using fluorine, chlorine or bromine plasmas. However, fluorine plasma is preferred because high etch rates can be achieved.

The introduction of inert argon gas enhances the etching by enhancing ion bombardment. However, it can lead to undesired hard mask damage. The addition of oxygen (~5%) to CF_4 and SF_6 plasmas can greatly increase the etch rate as it increases radicals density and prevents recombination [85]. Therefore, oxygen is typically introduced in majority of etching processes, although it ashes photoresist. The tailoring of pressure and power values results in different etch rates. Table **1** shows the etch rates of sputtered NbN using CF_4 plasma. As it can be seen, addition of oxygen increases the etch rate six times. Increased pressure has no effect on the etch rate. Higher power enhances etch rates as maximum by 14%.

Table 1. RIE of reactively sputtered NbN.

CF_4: O_2, sccm	Pressure, mTorr	Power, W	Etch Rate, nm/min
80:20	30	200	0.78
80:20	100	200	0.78
80:20	30	100	0.67
80:20	100	100	0.73
100:0	30	100	0.13
70:0	30	100	0.06

DRIE

Deep reactive ion etching (DRIE) is a modified reactive ion etching used to obtain higher etch rates, higher aspect ratios and thereby more complex microstructures than with RIE. It utilizes high-density plasma at low pressure ranges and two plasma sources [84]. The main technologies for DRIE are Bosch process and cryogenic process.

Bosch process

The Bosch process consists of alternating cycles: etching with SF_6 to form volatile etch products and passivation with C_4F_8 to form fluoropolymer ($(CF_2)_n$) on the sidewalls and bottom of the etched silicon structures (Figure 14). The following etch cycle removes the polymer from trenches by ion-assisted bombardment, exposing the bottom for the chemical etching. The polymer remains on the sidewalls protecting them from etching [12].

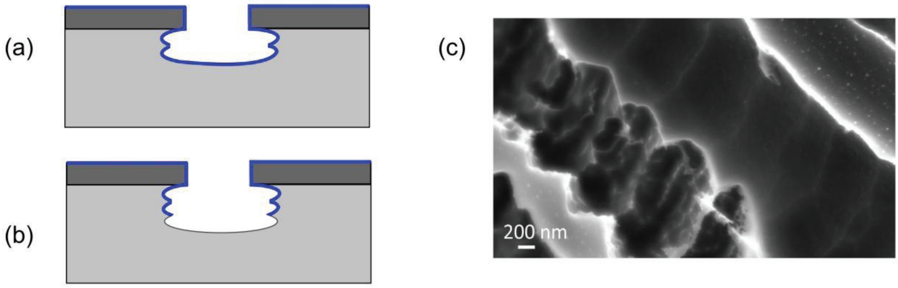

Figure 14. The Bosch process principle: (a) passivation step; (b) isotropic etching. (c) SEM micrograph of the silicon sidewalls after etching.

Each cycle lasts for several seconds. The repetition of etch-passivation cycles leads to vertical profiles. Short cycles provide smoother sidewalls, whereas long cycles provide higher etch rates.

In this thesis, the Bosch process (STS Advanced Silicon Etch) through the silicon wafer was performed with 139 sccm of SF_6, 98 sccm of C_4F_8 and 10 sccm of O_2 gas flows at 94 mTorr, 13.56 MHz rf frequency, 10 W platen power and 25°C chuck temperature: SF_6/O_2 etch step was 10 s, C_4F_8 passivation step was 6 s.

Cryogenic process

Cryogenic etching is conducted at low temperatures ranging from – 80 to – 140°C. At these temperatures, chemical reactions are minimized promoting anisotropic etching. Furthermore, in the cryogenic etching, the passivation and etching occur simultaneously. The process typically involves SF_6 and O_2. High percentage of oxygen (>15%) is introduced to yield a passivation layer (SiF_xO_y). Oxygen is needed to form the passivation layer which prevents lateral etching. Thin passivation layer (SiF_xO_y) forms and remains on the sidewalls. Ion bombardment proceeds in the vertical direction removing the passivation layer and thus vertical etching continues. Using these conditions it becomes possible to create high aspect ratio structures with vertical profiles with smooth sidewalls. Too high oxygen concentrations, however, lead to the black silicon formation.

Typically the increase of the etching process temperature increases etch rates, however it reduces anisotropy. Conversely, the etching does not occur at temperatures lower than – 140°C. This is due to condensation of SF_6 on the surface; this thick layer prevents physical etching by ions [87].

Sidewalls after DRIE

The presence of the passivation layer is crucial in DRIE. It allows achieving through-wafer etching or high aspect ratio structures with vertical sidewalls. However, sidewalls are often non-ideal.

During, cryogenic process, the excess of oxygen leads to positive sidewalls, whereas the excess of SF_6 leads to negative slopes [85]. Figure 15 shows the failure of silicon micropillars due to high SF_6/O_2 ratios during DRIE. As also visible from micrograph, the following increase of oxygen led to formation of black silicon spikes.

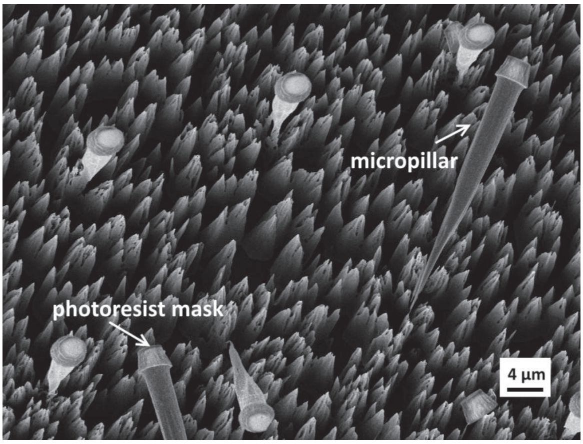

Figure 15. SEM micrograph of failed micropillars due to negative slopes.

The Bosch process exhibits scalloping, which makes the process inappropriate for certain optical applications, e.g., mirrors or waveguides. The reduction of scalloping can be achieved by shortening the lengths of passivation and etching pulses or by simultaneous injection of them both. However, etch rate is reduced [86].

The quality of sidewalls is an issue for many MEMS devices because it affects to mechanical robustness and strength of a whole device. Rough sidewalls can induce silicon cracking and reduce the fabrication yield. Annealing in hydrogen can be employed to improve sidewalls quality and/or to reduce scalloping of the Bosch process [88]. The smoothening effect is related to enhancing of silicon surface atoms mobility at high temperatures. Silicon atoms migrate on the surface to minimize the surface energy. This leads to smooth profiles [88]. Alternatively, isotropic plasma etching after DRIE can improve the quality of sidewalls. Isotropic plasma removes irregularities, reduces the roughness and therefore increases the mechanical strength [12].

The mechanical strength of silicon sidewalls is extremely sensitive to process conditions because surface quality determines their strength. The strength of silicon sidewalls was determined by loading the half-etched hub structures (micropillar) from the flat surface by Chen, *et. al* [89,90]. The highest strength of etched silicon walls was of 4.6 GPa, when etching was performed with the Bosch process. Wet etching in potassium hydroxide reduced sidewalls strength to 3.4 GPa. It was also concluded that after DRIE high surface roughness leads to low, but uniform sidewalls strength. In contrast, low surface roughness leads to high strength, but with great scatter.

DRIE process temperature

Process temperature is a critical parameter influencing sidewall quality. Small temperature fluctuations yield wavy sidewalls. Figure 16 shows wavy sidewalls of the etched silicon pillar caused by process temperature drift. If temperature rises, more lateral etching can take place. Therefore, to obtain perfectly vertical sidewalls, it is essential to keep process temperature nearly constant.

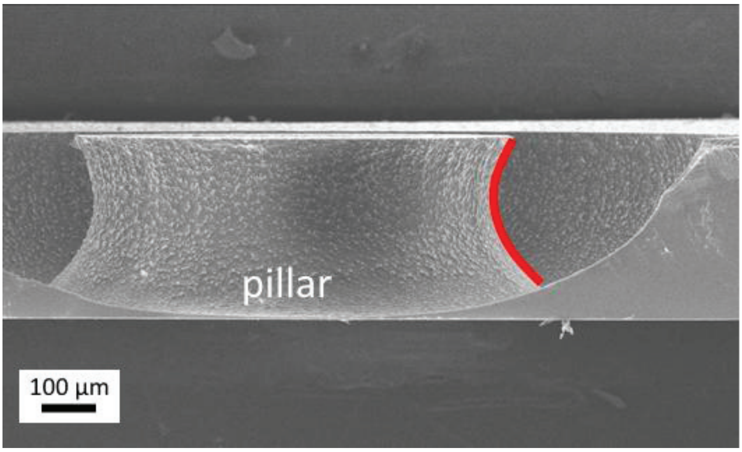

Figure 16. Wavy profile of micropillar due to process temperature fluctuation.

RIE lag and aspect ratio dependent etching

In reactive ion etching, larger opening areas etch faster than narrow gaps when aspect ratio exceeds 1:1. The effect is called RIE lag. Therefore, complex structures or features of different dimensions cannot be optimized simultaneously. Another similar issue is aspect ratio dependent etching: reduction of the etch rate with time. Both effects are associated with depletion of etchants at the bottom of the narrow features and with difficulty of removal of volatile byproducts from narrow trenches [91,92]. These non-idealities can be reduced by reducing the process pressure to supply more etchants and to remove volatile byproducts more effectively.

RIE lag is important to take into account when designing a pattern for test structures. It is essential that mask for patterning contains structures, e.g., membranes, of similar areas. Otherwise, structures with larger opening areas can be even destroyed by ion bombardment while structures with smaller areas remained unreleased.

Aspect ratio dependent etching issue is important to consider during dry etch release. Careful control of etch rate is needed to avoid over- or under-etch.

Notching (footing)

Notching effect appears when high density plasma reaches the etch stop oxide layer and, as a result, charge accumulates at the insulator. The charge repels incoming ions to the sidewalls causing damage of the silicon/insulator interface. The suppression of notching (charge neutralization) is possible by pulsing of substrate bias power to alternate electric field [86].

When fabricating free-standing structures, notching can cause the variation of the designed geometry with obtained one, i.e. increasing sample area. Therefore, one should employ microscopy to evaluate the dimensions of a sample after dry etch release.

Hard masks

The etch mask must be made out of material which can tolerate plasma with minimum losses. Photoresist is prone to crack at cryogenic temperatures and moreover it is not durable enough for deep structures. The selectivity of photoresist can reach 150:1 and 3-5:1 in fluorine and chlorine plasmas, respectively [12]. Besides photoresist, hard masks like thermal silicon dioxide or aluminum oxide can be used to obtain high selectivity. Thermal silicon dioxide is grown typically at high temperature, i.e. 1000°C, which limits its utilization as an etch mask. Sputtered aluminum oxide exhibits 1:5,000 selectivity to silicon [93], whereas selectivity of ALD aluminum oxide to silicon is 1:66,000 [94]. Even 1 nm of ALD Al_2O_3 is enough to act as a hard mask [95]. Thus extra thin layers of Al_2O_3 are very attractive for variable applications where high selectivity is required (Publications **I, II, III, IV**). In contrast, ALD TiO_2 is less suitable as a hard mask for DRIE. It is etched with CH_xF_y and SF_6 plasma exhibiting high variation in etch rates [96]. Figure 17 shows the surface after TiO_2 etching using SF_6 plasma. As can be seen from the figure, no masking layer remains on the surface. The etching results in rough black silicon surface.

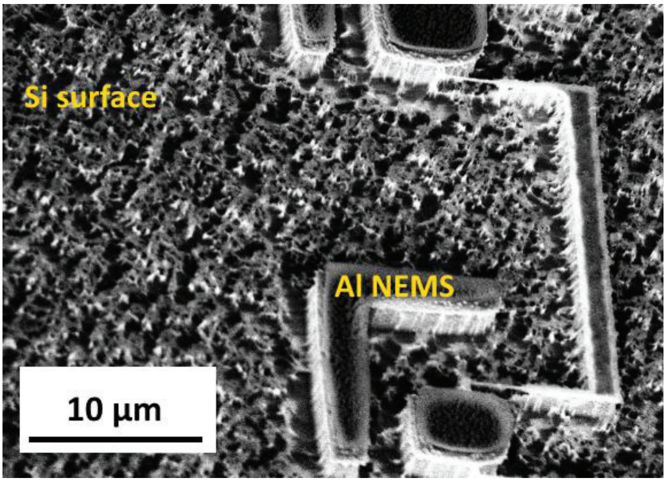

Figure 17. SEM images shows that ALD TiO_2 layer as a mask was consumed and underlying silicon was exposed to SF_6 plasma etching, resulting in silicon nanograss.

DRIE for free-standing structures

A great advantage of dry etching, in contrast with wet etching, is a possibility to fabricate various shapes independent of crystal planes (Publications **I, II, III, IV**). Typically, membrane fabrication requires etch through the substrate open areas until etch stop layer is reached (bulk micromachining). Therefore, it is desired to have a good etch stop layer. The main requirement for it is a good selectivity: during DRIE etch stop layer must tolerate plasma without being damaged. Figure 18 shows ALD Al_2O_3 circular and oval membranes (used as MEMS test structures). ALD Al_2O_3 was used as an etch stop layer, as a functional device layer (top side of the wafer) and as a hard mask (bottom side of the wafer).

The fabrication process of free-standing structures using ALD Al_2O_3-based materials is straightforward: after deposition of ALD Al_2O_3, the backside of the substrate is patterned to define opening areas using lithography and wet etching in BHF. BHF etches alumina with no impact to silicon. Next, DRIE continuous until free-standing structure are released. ALD Al_2O_3 films tolerate SF_6-based plasma, however, careful control is required to avoid any membrane damage by ion bombardment.

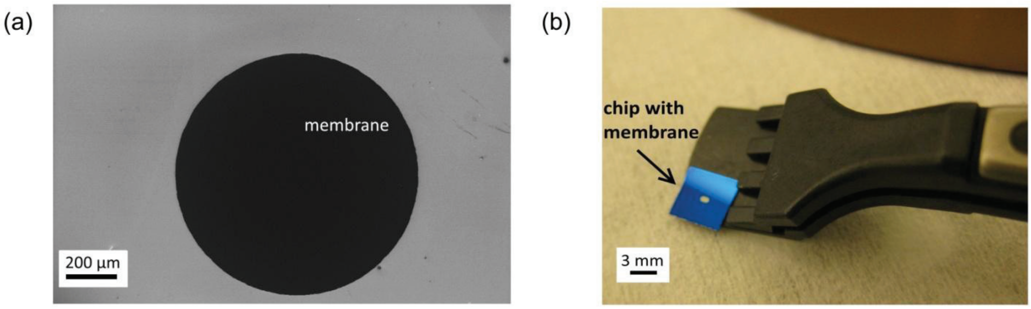

Figure 18. ALD Al_2O_3 (a) circular and (b) oval free-standing membranes.

This approach was used in the majority of experiments in this thesis. The etching was performed with a carrier wafer to keep chips with membranes on top of that. The fabrication process flow of samples used in Publications **I, II, III, IV** (Figure 19) contains following steps:

1. Wafer selection (double-side polished (DSP) silicon, 310 µm) and wafer surface cleaning in RCA2.
2. ALD deposition of Al_2O_3 (top side).
3. ALD deposition of Al_2O_3 with the thickness of 20 nm (bottom side).
4. Lithography.
5. Photoresist spin coating on the TOP side to protect the actual test structures.
6. Etching of 20 nm Al_2O_3 from the BOTTOM side by BHF at 32°C for 30 sec.
7. Removal of the photoresist.
8. Etching of silicon using the Bosch process.

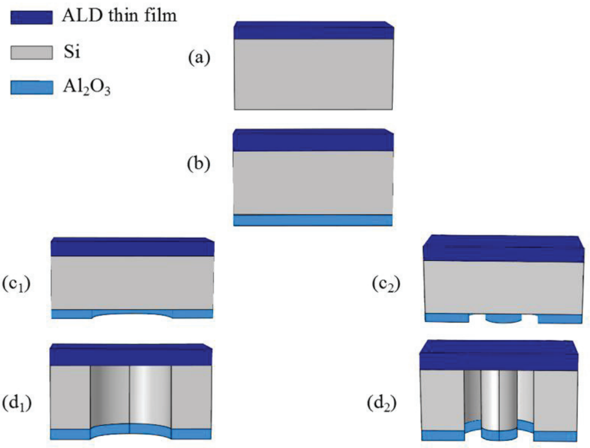

Figure 19. Fabrication steps of test structures. (a) ALD thin film to test and as etch stop layer; (b) backside ALD Al_2O_3 as etch mask; (c_1), (c_2) etching of ALD Al_2O_3 from the back side (d_1), (d_2) through-wafer etching by Bosch process (Publication **I**).

It is important to mention that release of ALD Al_2O_3-based membranes of smaller thickness than 50 nm should be preferable finished with mild RIE SF_6-based etch. Thinner membranes may be more susceptible to damage by physical ion etch. However, in this method, the dimensions of membranes will be lost due to isotropical nature of low power RIE. Alternative approach was developed by Wang L., *et. al.* [97], by growing ALD Al_2O_3 films on suspended graphene. Graphene monolayer was removed by oxidative etching (at 600°C for 10 hours) to obtain only free-standing Al_2O_3 membranes. This method resulted in release of 1-nm thick free-standing membrane but the membrane diameter was only 5.52 μm.

5) Annealing of thin films

Annealing is a thermal treatment used for several purposes: to active dopants, to modify bonds of bonded wafers, to densify films and to reduce residual stress in materials.

Annealing changes physical and chemical properties of thin films since annealing induces modification of film composition, reduction of pin-holes, increasing of grain sizes. Therefore, annealing influences the crystallinity and to the mechanical properties of materials. However, if thin film is deposited at temperatures comparable to the annealing temperature, then only minor residual stress changes can be observed after annealing. This is associated due to low thermal stress induced by annealing. For instance, LPCVD films have stable tensile stress during and after annealing. In contrast, if films are grown at lower temperatures than of annealing and have different expansion coefficients from a substrate, dramatic stress changes can take place. For example, the residual stress of PECVD silicon oxide films after annealing >800 °C become more compressive since the thermal expansion coefficient of silicon oxide is much lower than of silicon substrate (3.08 ppm/°C for silicon versus 0.55 ppm/°C for silicon oxide) and therefore the film is unable to shrink as much as silicon during cooling to room temperature, leading to compression of the film. If annealing of PECVD silicon oxide is performed at 500–550°C, then most of hydrogen and moisture diffuse out, and film can even experience tensile stress due to microstructure changes induced by hydrogen reduction from the film. PECVD silicon nitride films exhibit different behavior from PECVD silicon oxide upon annealing at temperatures >600°C due to very small difference of thermal expansion coefficients with silicon (the difference is only 0.8 ppm/°C). During the annealing, silicon nitride film losses hydrogen and stress rapidly changes from compressive to tensile and stays tensile after the cooling to the room temperature [98]. Figure 20 displays schematic representation of the mechanism of hydrogen loss in PECVD Si_3N_4 film during annealing. The weakest SiH bonds break along with NH bonds. This is followed with hydrogen diffusion from metastable sites to the surface of the film or to the interface. This effect forces neighboring silicon and nitrogen atoms to form new SiN bonds.

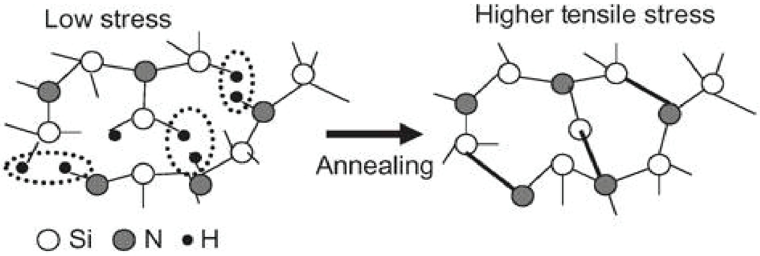

Figure 20. Schematic representation of possible mechanism of hydrogen loss in PECVD Si_3N_4 film during annealing (from [98]).

Annealing provokes self-diffusion and diffusion between different layers. For example, annealing of free-standing Au/Cr/Si beams [99,100] causes microstructural evolution of gold layer. The thermal treatment results in grain growth of the gold layer, changing curvature of beams and stress level. The effect is due to inter-diffusion of underlying chromium to gold, and self-diffusion of gold. An additional ALD Al_2O_3 layer can prevent the self-diffusion of the gold and inter-diffusion of chromium. The use of aluminum oxide, as a result, helps to block the abnormal gold grain growth.

Annealing of ALD Al_2O_3 films

Due to its excellent passivation properties, ALD Al_2O_3 is widely used in solar cells for surface passivation, where thermal treatment (firing at temperatures higher than 400 °C) is one of the key fabrication steps [101-104]. However, annealing can influence mechanical properties, composition and adhesion [33]. Therefore, one of the goals of this thesis was to analyze the changes of properties of ALD Al_2O_3 films induced by thermal treatments. Annealing was performed at atmospheric pressure in an oven (PEO–601) and at vacuum of 7 mbar in a rapid thermal process furnace (Jipelec RTP), both at 500 °C, 600 °C and 700 °C for 20 min in nitrogen environment.

Annealing of Al_2O_3 films deposited with TMA and H_2O/O_3 precursors caused blistering of the films [105], as shown in Figure 21.

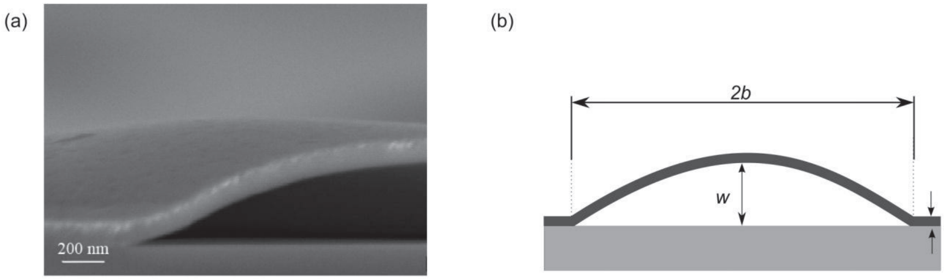

Figure 21. (a) Cross-section of a blister of ALD Al_2O_3 after annealing. (b) Schematic cross-section of the blister.

Figure 22 displays heights, diameters and densities of annealed ALD Al_2O_3 films deposited on silicon substrate at 220°C. Atomic force microscopy was performed to analyze geometries of blisters. All samples showed blisters after 500°C or higher annealing temperatures independent of deposition and annealing conditions. The blister heights increased with the annealing temperatures for all ALD processes, whereas diameters remained roughly the same. The blister densities did not exhibit any trend. Ozone pretreatment for 5 min was done to improve the uniformity and conformality of the interfacial oxide layer. As can be seen from the Figure 22, ozone pretreatment led to smaller blisters, but with the highest density. TMA-water based Al_2O_3 (without ozone pretreatment) films had larger blister heights and diameters than all other processes. Aluminum oxide grown with TMA and O_3 behaved similarly to other deposition processes.

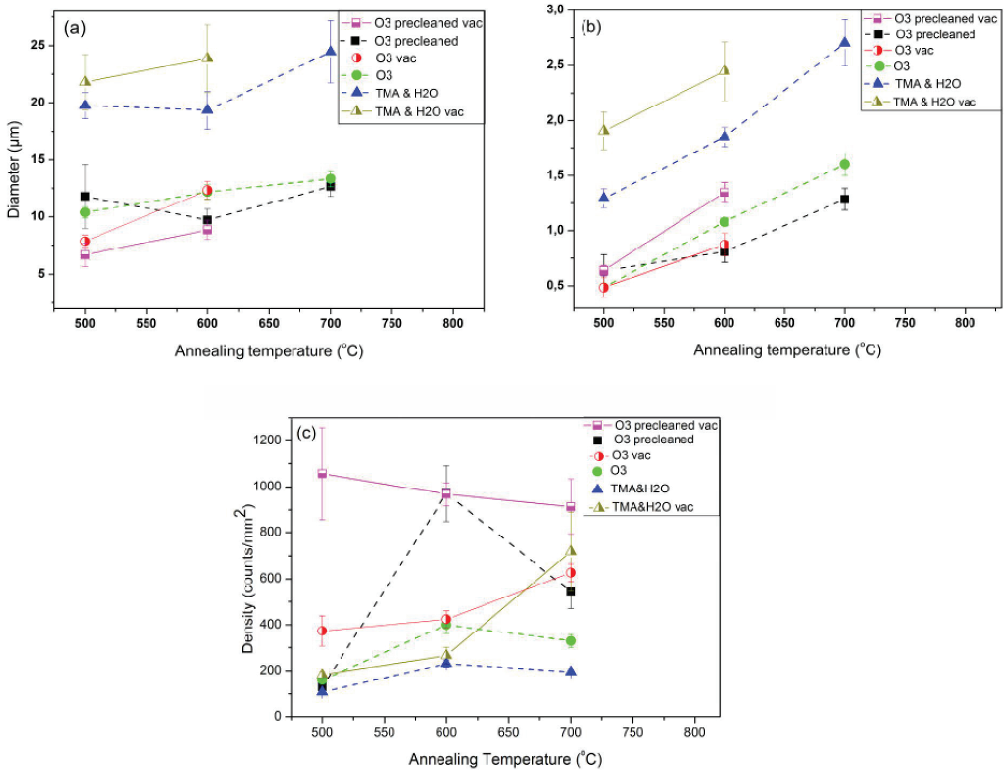

Figure 22. (a) Blister diameters and (b) blister heights versus annealing temperature measured by AFM; (c) blister density versus annealing temperature determined by digital image analysis. Vac refers to vacuum annealing.

Annealing in vacuum resulted in larger blister heights than annealing in atmospheric pressure. In case of annealing in vacuum at 700°C, blisters underwent fracture. The blisters grew until the moment of maximum strain, and then they broke. In case of annealing of free-standing membranes, membrane areas were blister-free, whereas blisters were formed only at the silicon/Al_2O_3 interface (Figure 23).

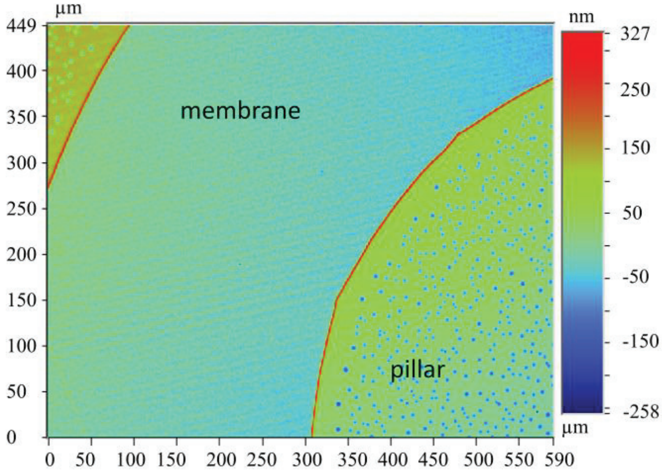

Figure 23. Optical profilometer (Veeco) scan of free-standing ALD Al_2O_3 membrane showing blistering effect revealing on silicon surface. No blisters on membrane, blistering on silicon.

The quantitative composition and impurities analysis of the annealed ALD Al_2O_3 thin films was done by TOF-ERDA with 8.515 MeV $^{35}Cl^{4+}$ incident beam. The TOF-ERDA measurements indicated the changes of composition in the films (Table 2). The impurity concentrations were, however, both process and annealing temperature dependent. There was more hydrogen in the film with H_2O process than with O_3 process. Ozone pretreatment seemed to reduce hydrogen. All films had very low carbon content (<1%), which did not change after annealing. Carbon concentration was higher with O_3 process. As can be seen from the table 2, hydrogen concentration decreased after annealing independent of chosen precursor. Aluminum concentration was independent of deposition conditions and remained stable after annealing. The [O]/[Al] ratio was slightly over stoichiometric value (>1.5), indicating that films had the excess of oxygen. The [O]/[Al] ratio, i.e. oxygen concentration, was reduced after annealing. For example, for TMA and O_3 process, the oxygen loss after annealing was only 0.07 at.%. Thus the total amount of water lost then is 0.14 at.% from total hydrogen loss of 1.70 at.%. Therefore, the blistering formation mechanism can be likely related to accumulation of the trapped hydrogen gas and water at the interface. Perhaps hydrogen and water diffused from the Al_2O_3 film to the local spots of adhesion loss, i.e. interfacial microvoids. In case of membrane, gaseous H_2O and H_2 diffused easily away. Thin films with ozone pretreatment, however, appeared to have only hydrogen out-diffusion. Moreover, stoichiometry increased after annealing. After annealing, blisters had the smallest sizes for the samples with ozone pretreatment. Perhaps the interfacial layer tends to prevent the diffusion of water to the interface, reducing dimensions of blisters. We performed additional annealing at 600 °C for 20 min of ALD Al_2O_3 (TMA and H_2O process) on thermal oxide (>1 µm thick) to investigate if blistering can take place with the additional barrier layer. As a result, no blisters were observed at the interface showing that most likely thermal oxide acts as hydrogen diffusion barrier.

According to our XRR results, the thickness values decreased as the annealing temperature increased (Table 2). For example, the thickness decreased by 15% after annealing in vacuum at 700 °C. There were, however, no significant material losses observed as the density increased coincidentally by 15%. The thickness reduction can be attributed partly to densification of Al_2O_3 film and to changes in its composition, i.e. hydrogen and water diffusion.

Annealing causes degradation of the adhesion of Al_2O_3 layer (blistering), therefore energy released to form a blister can be determined. The interfacial fracture energy for blisters $W_{ad,p}$ is defined by the critical buckling stress σ_b and the driving stress σ_d [14,15,106,107] as follows

$$Wad,p = \left[\frac{(1-v^2)h}{2E} (\sigma_d - \sigma_b)(\sigma_d + 3\sigma_b) \right]. \qquad (11)$$

Table 2. XRR and TOF-ERDA results. Density and thickness variations upon annealing (XRR). Atomic concentration of impurities present in Al_2O_3 thin films before and after annealing (TOF-ERDA).

Sample: annealing	Density (g/cm^3)	Thickness (nm)	Hydrogen (at. %)	Carbon (at. %)	Oxygen (at. %)	Aluminum (at. %)	Oxygen/Aluminum ratio
Reference, TMA and O_3	3.00	83.5	1.78±0.08	0.69±0.05	60.1±0.4	37.4±0.3	1.61
500 °C atm, TMA and O_3	3.08	82.5	1.51±0.07	0.69±0.04	59.7±0.4	38.1±0.2	1.57
600 °C atm, TMA and O_3	3.02	81.5	0.44±0.05	0.66±0.05	60.5±0.5	38.4±0.3	1.57
700 °C atm, TMA and O_3	3.08	81.0	0.08±0.03	0.81±0.07	60.1±0.5	39.0±0.4	1.54
500 °C vac, TMA and O_3	2.95	82.5	--	--	--	--	
700 °C vac, TMA and O_3	3.50	70.0	0.05±0.02	0.61±0.04	60.7±0.4	38.6±0.3	1.57
Reference, TMA and H_2O	3.00	96.7	2.5±0.1	0.17±0.03	59.3±0.5	38.0±0.3	1.56
700 °C atm, TMA and H_2O	3.05	94.7	0.18±0.04	0.15±0.03	60.2±0.5	39.5±0.4	1.52
Reference, O_3 pretreatment, TMA and H_2O	3.00	92.7	2.1±0.1	0.15±0.03	59.4±0.5	38.4±0.3	1.55
500 °C atm, O_3 pretreatment, TMA and H_2O	--	--	1.65±0.10	0.14±0.02	60.2±0.5	38.0±0.3	1.58
700 °C atm, O_3 pretreatment, TMA and H_2O	3.05	91.7	--	--	--	--	--

The critical buckling stress and the driving stress depend on the film thickness *h*, the radius *b* and height of the blister *w* (Figure 21 b)

$$\sigma_b = \frac{\pi^2 E}{12(1-\nu^2)}\left(\frac{h}{b}\right)^2, \qquad (12)$$

$$\sigma_d = \sigma_b\left[\frac{3}{4}\left(\frac{w}{h}\right)^2 + 1\right], \qquad (13)$$

where E is the Young's modulus, and ν is the Poisson's ratio.

The blister dimensions were measured using AFM to calculate the interfacial fracture energies between ALD Al_2O_3 and silicon substrate. Table 3 summarizes the interfacial fracture energies evaluated by Equation (11). As can been seen, interfacial fracture energies linearly increased as a function of annealing temperature due to hydrogen and water diffusion to the interface. Thin films deposited by TMA and H_2O had the highest interfacial fracture energy. The O_3 pretreatment seemed to improve the interfacial strength, i.e. reduce local spots of adhesion loss.

In addition to blistering effect, annealing slightly tailored the residual stress of ALD Al_2O_3 films. As it has been shown in our work [104], the thermal expansion coefficient for Al_2O_3 is only slightly higher than for the silicon substrate (3.84 ppm/°C for ALD Al_2O_3 and 3.08 ppm/°C for silicon). Thus hydrogen and water diffusion is most likely a dominating mechanism of changes in the residual stress. After thermal cycling to 500°C with rate of 10 °C/min, the residual stress of ALD Al_2O_3 films increased from 308.1 MPa to 341.5 MPa.

Table 3. Interfacial fracture energies of annealed ALD Al_2O_3 (Eq. 11)

Sample: precursors	Annealing temperature (°C)	Interfacial fracture energy (J/m^2)
TMA and O_3	500	0.26±0.08
TMA and O_3	600	2.87±0.86
TMA and O_3	700	9.13±1.56
TMA and H_2O	500	0.96±0.17
TMA and H_2O	600	4.57±1.53
TMA and H_2O	700	10.77±2.84
O_3 pretreatment, TMA and H_2O	500	0.47±0.09
O_3 pretreatment, TMA and H_2O	600	2.48±0.44
O_3 pretreatment, TMA and H_2O	700	5.61±1.61

5. Characterization of residual stress, elastic modulus and fracture strength

5.1. MEMS devices as tools for thin film mechanical characterization

MEMS devices can serve as micro-test structures to measure mechanical properties of thin films. Typically MEMS test sample represents a free-standing structure manufactured by bulk or surface micromachining. Each device is clamped from one or two sides as designed prior the fabrication. Among MEMS test structures are: single supported beams, doubly supported beams, and membranes (Figure 24).

The reliable measurement of mechanical properties depends on many challenging issues related to sample preparation, assembling, handling, determination of dimensions, and precise application of load to deform samples [108]. Prior to the actual measurement, the sample has to be positioned and aligned with respect to loading using, for example, an optical microscope. If microscope optics is included in the set-up, then it can be used for further optical characterization. Atomic force and electron microscopy can be, in addition, used to study *in-situ* changes in surface topography and microstructural deformation during loading.

Typically, the mechanical load is done with an indenter tip and electrostatic MEMS actuators. Fragile, thin samples can easily break when loaded with a sharp tip. Sharp contact induces severe deformation at the point of loading and consequently cracks start to develop. Therefore, to avoid premature fracture it is essential that the tip is round and smooth. Alternatively, the loading mechanism can be fabricated along with sample to accurately apply mechanical load to the certain position of a specimen.

The important requirement for successful material characterization is to determine carefully specimen dimensions. Dimensions of the test structure can be measured with optical and electron microscopy, profilometry or interferometry before and after the actual measurement. The optical analysis of the sample after measurements gives information about cracking and sample deformation.

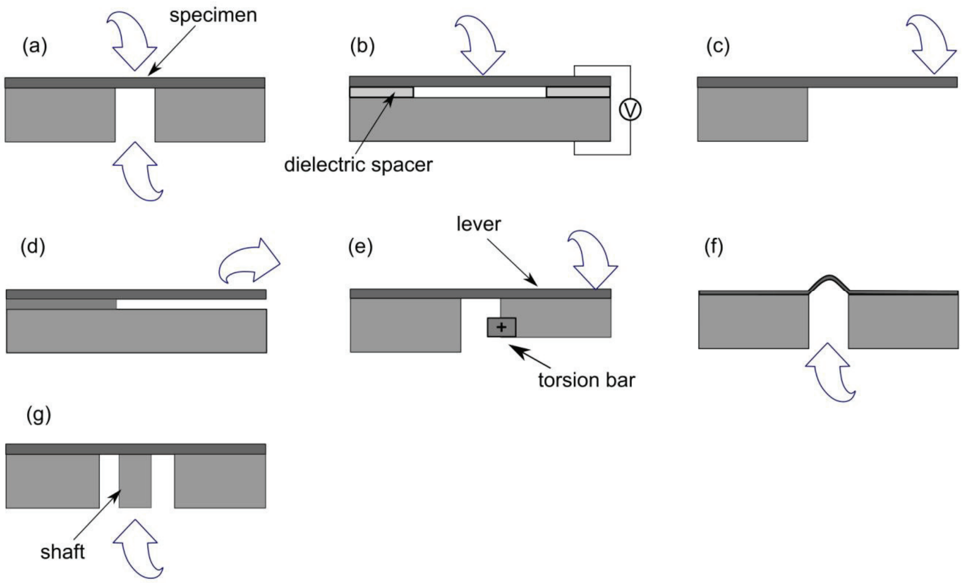

Figure 24. MEMS devices used to measure mechanical properties: (a) beam bending; (b) M-test; (c) cantilever beam bending; (d) tensile test; (e) tensile test with integrated load mechanism; (f) bulge; (g) MEMS shaft-loaded test methods.

In the *beam (microbridge) bending* (Figure 24 (a)), mechanical load is applied to the beam center [109]. The load can be applied from different directions depending test on configuration. The Young's modulus E and residual stress σ_o are extracted from analysis of load-displacement curves (Figure 25) and geometry of the specimen. The tensile stress is obtained as a ratio of the applied force to cross-sectional area of the beam, and the intercept with stress-axis refers to the residual stress. The Young's modulus is evaluated as the relationship between tensile stress σ and corresponding tensile strain ε. Fracture strength is measured as the maximum tensile stress the beam can withstand.

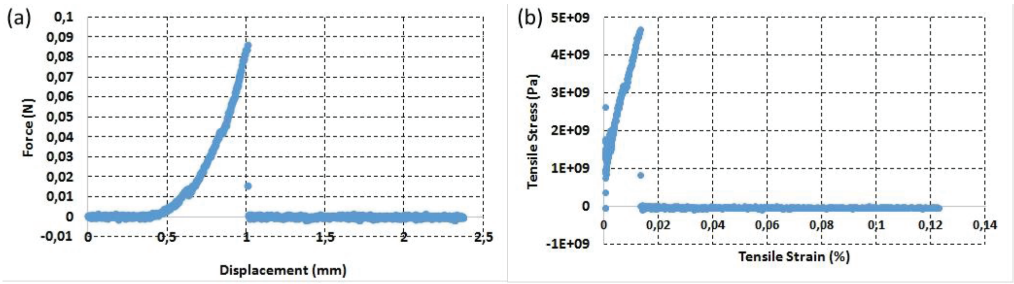

Figure 25. (a) Force-displacement and (b) corresponding stress-strain curves obtained from beam (carbon fibers covered with ALD films [110]) bending measurement.

The main challenge in the measurement is to apply the load to the center of the beam. Misalignment leads to high scatter in the results, unwanted bending moment or premature sample failure. Therefore, the loading force, specimen, and microscopy have to be all in precise alignment. Advantages include simple sample preparation and relatively easy data analysis.

The electrical response of MEMS structures is related to material properties. Therefore, the residual stress and Young's modulus can be also obtained from the analysis of the beam bending under applied voltage: M-test (Figure 24 (b)) [111]. The applied voltage is expressed as follows

$$V = \sqrt{\frac{\gamma_{1n} S}{\varepsilon_0 L^2 D_n(\gamma_{2n}, k, L)[1 + \gamma_{3n} \frac{g_0}{b}]}}, \tag{14}$$

where ε_o is the air permittivity, g_o is the initial gap between the film with the thickness h and ground electrode, b is beam width, L is beam length or plate radius, $\gamma_{1n\text{-}3n}$ are fitting parameters, index n =1 refers to cantilevers, n = 2 to beams, and the parameters defined as $k = \sqrt{12S/B}$, $S = \hat{\sigma} h w^3$, $B = Eh^3w^3/(1-\nu^2)$ (ν is the Poisson's ratio) and

$$D_n = 1 + \frac{2[1 - \cosh \gamma_{2n} \frac{kL}{2}]}{(\gamma_{2n} \frac{kl}{2}) \sinh(\gamma_{2n} \frac{kl}{2})}. \tag{15}$$

Therefore, the extraction of the parameters S and B give a measure of mechanical material properties [111]. The effective stress $\hat{\sigma}$ is equal to zero for cantilevers, whereas for beams it defines as $\sigma(1-\nu)$. To obtain precise material mechanical properties it is necessary to evaluate carefully the thickness, radius of the sample, gap dimensions, and bending deformation (curvature) of buckled beam or cantilever. Large dimensions can be problematic due to possible stiction or residual stress related issues.

In *cantilever beam testing*, a free-standing beam fixed from one end is subjected to mechanical bending load F until the beam is broken (Figure 24 (c)). An indenter tip or electrostatic MEMS actuators are used as the loading devices with very high force resolution. The beam displacement w is recorded as a function of load, leading to corresponding stress-strain curves and therefore to extraction of mechanical properties.

The Young's modulus, residual stress and fracture strength can be defined as follows [112,113]

$$E = \frac{4(1-\nu^2)L^3}{bh^3}\frac{F}{w}; \tag{16}$$

$$\sigma_0 = \frac{E_s}{(1-\nu_s^2)} \frac{wh_s^2}{3(L^2 + w^2)h}, \tag{17}$$

$$\sigma_f = \frac{6LF^*}{bh^2} \tag{18}$$

where E_s, h_s and ν_s are the substrate Young's modulus, thickness and Poisson's ratio, F^* is the maximum fracture load, L is the effective length (distance from the fixed end to the point where the load is applied), b is the width, h is the thickness of a cantilever beam.

Another configuration is when the thickness of the cantilever reduces gradually along with length. In this case, the Young's modulus is obtained as [114]

$$E = \left(\frac{F}{w}\right)\left(\frac{6(1-v^2)}{bm^3}\right)\left[2\ln\left(1+\frac{mL}{t_t}\right) - \frac{mL(3mL+2t_t)}{(t_t+mL)^2}\right], \quad (19)$$

where t_t is the thickness at the point of loading, and m is the thickness gradient.

During *tensile testing*, a beam is pulled until fracture event (Figure 24 (d)). To facilitate pulling, the sample typically contains a mechanical movable grip [115,116]. It is, therefore, important to ensure that mechanical gripping does not damage the specimen. Furthermore, the test structure can experience high stress at gripping. The most reliable configuration uses a specimen containing a test structure between a fixed end and pull ring. This ring is then laterally loaded by inserted into the ring nanoindenter ("pull-tab") [117,118]. This configuration avoids misalignment between gripping and the test structure. During tensile testing, the gripper displacement is measured to obtain tensile strain, and corresponding pulling force per cross-sectional area is defined as tensile stress.

The fracture strength is expressed as [119]

$$\sigma_f = \frac{3LF^*}{4hb^2}. \quad (20)$$

A tensile testing with integrated loading mechanism to a specimen (Figure 24 (e)) reduces a number of problems associated with alignment or gripping. The MEMS test device consists of specimen, loading lever, torsion bars, and a supporting frame. When the perpendicular load is gradually applied, the specimen film stretches in the horizontal directions as the lever rotates around the axis of torsion bars. The tensile stress is obtained as a function of applied load, subtracting the repulsive force of the torsion bars. The subtraction of the repulsive force is done with an addition lever loading after the sample fracture. The tensile strain is determined from the analysis of angular rotation of the lever. Often it is difficult to measure the beam elongation and to extract strain and Young's modulus values. In this case "differential stiffness" approach is used. The Young's modulus defines from two samples with the same width, but with different lengths L_1 and L_2

$$E = \frac{S_1 S_2 (L_1 - L_2)}{A(S_2 - S_1)} \quad (21)$$

where S_1 and S_2 refers to beams' stiffness (defined as the ratio of tensile force to the displacement of loading mechanism), and A is the beam cross-sectional area [120].

In the *bulge technique* (Figure 24 (f)), the uniform overpressure P is applied to a free-standing membrane, creating an out-of-plane deflection w of the membrane. This deformation is monitored as a function of applied overpressure to analyze material mechanical properties. This method eliminates problems with possible premature fracture of very thin films by indenter contact. The extraction of mechanical properties is achieved by analyzing pressure-deflection behavior of suspended membrane upon its pressurizing (Publication **I,** Publication **III**). The membrane profile upon pressurizing can be obtained with the SWLI measurement (Figure 26). Each time when overpressure is applied, the membrane profile is SWLI scanned and precise values of deflection is recorded (Publication **I**, Publication **III**).

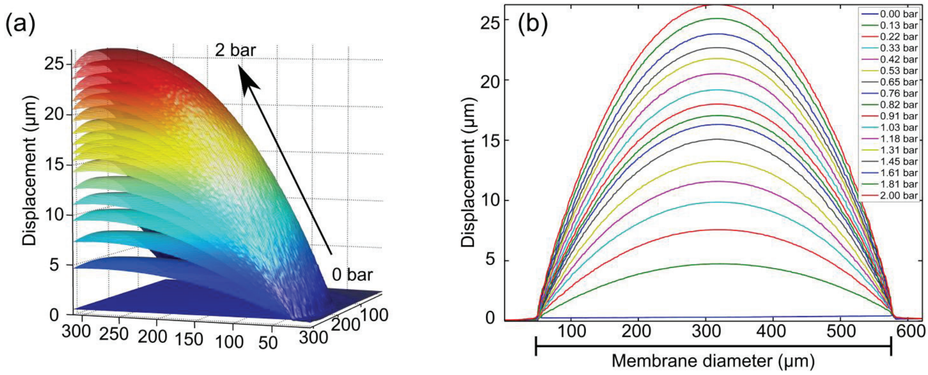

Figure 26. SWLI measurement: the extracted profile of pressurized 100 nm-thick ALD Al_2O_3/graphene/Al_2O_3 membrane.

The general equation that relates overpressure *P* to the deflection *w* of a membrane follows cubic law and is defined as [121]

$$P(w) = C_1 \frac{h\sigma_0}{a^2} w + C_2 \frac{hE}{a^4(1-\nu)} w^3 . \tag{22}$$

where *h* is the film thickness, *a* is the radius of suspended membrane. The material mechanical properties, such as the Young's modulus and residual stress, can extracted by the fitting the experimental data to the bulging Equation (22). C_1 and C_2 depend on membrane shape, and analytical model used (Table 4). Many models have been proposed to extract the coefficients [121-127]. For circular membranes, the coefficient C_1 is in a good agreement for every model. For example, the model proposed by Beams [123] assumes no dependence of C_2 on the Poisson's ratio, and it assumes that stress and strain are equi-biaxial everywhere in the film. Other models, in contrast, include strain variation from biaxial strain at the center to the plane strain at the edges. These assumptions result in variations of C_2 with ν [122].

Table 4. Values of C_1 and C_2 for membranes with different shapes.

Geometry	**C_1**	**C_2**	**Authors [reference]**
Circular	4.0	2.67	Beams [123]
Circular	4.0	(7-v)/3	Vlassak and Nix [124]
Circular	4.0	2.67(1.026+0.233v)$^{-1}$	Pan, *et. al.* [125]
Square	3.04	1.473(1-0.272v)	Tabata, *et. al* [126]
Square	3.41	1.37(1.075-0.292v)	Pan, *et. al* [125]
Square	3.393	(0.8+0.062v)$^{-3}$	Vlassak and Nix [124]
Square	3.45	1.994(1-0.27v)	Maier-Schneider, *et al.* [127]
Rectangular	1.552	[30/(1+v)][0.035-(16/(800-89 v))]	Tabata, *et. al* [126]
Rectangular	2	8/[6(1+v)]	Vlassak and Nix [124]

The fracture strength is determined from the rupture pressure P_u [128] by

$$\sigma_f^3 = \frac{1}{24}\frac{EP_u^2a^2}{(1-\nu)h^2} \ . \tag{23}$$

The main challenges in the bulge method are handling of samples and assembling them to the sample holder. Any pressure leaks lead to spurious data. Therefore, the sample holder has to be carefully designed and assembled. The bulge method is very sensitive to accuracy of characterization of dimensions and bulge height. Interferometry (e.g., SWLI) offers high accuracy of geometrical parameters measurement with nm-scale resolution. Circular, square, rectangular membranes can be studied. However, the yielding behavior of non-circular membranes is non-uniform, and therefore the data analysis can be problematic. Often it is desired to perform modeling to obtain proper analytical equation, and therefore precise mechanical characteristics.

MEMS shaft-loaded testing (MEMS SLT) is a recent technique, which we developed to characterize fracture and elastic properties of suspended thin films. During the measurement, the suspended membranes are stretched by applying a load to the center of an axisymmetric shaft (Publication **I,** Publication **IV**). The film is then gradually deflected until its fracture. In the MEMS SLT method, micro or nanoindenter actuates each shaft, which, as a result, stretches membranes. During each measurement, the shaft displacement is measured as a function of applied load. From these measurements, mechanical properties of thin films are evaluated. The load-deflection relationship can be defined from the analytical model, which is based on equi-biaxial stress approximation: when the tangential stress is equal to radial [129].

$$F = \frac{2\pi h\sigma_0}{\log\left(1/\zeta\right)}w + \frac{1}{\left(1-\zeta^2\right)\log^2(\zeta^2)}\left(\frac{4\pi Ehw^3}{(1-\nu^2)a_1^2}\right) \tag{24}$$

where $\zeta = c/a_1$ is the contact region of the shaft (c is the shaft radius, a_1 is the total radius of the membrane including shaft). Equation (24) assumes that no delamination occurs between the shaft and thin films and between the substrate and thin film to test (ζ is constant). The load-deflection data is correlated to the analytical model (Equation (24)) to extract Young's modulus and residual stress (Figure 27).

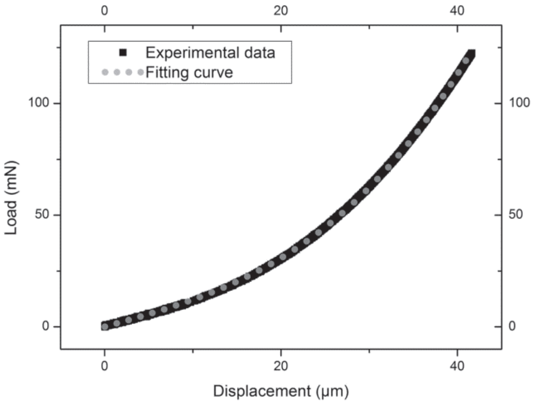

Figure 27. Load-displacement data and corresponding fitting curve using Eq. (21), shown for 200 nm-thick ALD mixed oxide $Al_xTi_yO_z$ film. (Publication **I**).

The fracture strength can be defined from maximum force of fracture and corresponding maximum displacement as follows

$$\sigma_f = \frac{F^* \log\left(1/\zeta\right)}{2\pi h w_{\max}}. \qquad (25)$$

A great advantage of the method is that the shaft is integrated into membrane. This method thereby alleviates the difficulty of loading and aligning of the load to the membrane center. This method can use commercially available equipment to apply the load to the shaft, e.g., microindentation. Therefore, it becomes possible to preset the loading position, maximum load, and approach and load speeds of indenter. However, prior to that, the geometry of each sample, i.e. film thickness, shaft and membrane widths, has to be evaluated. Furthermore, inaccuracy of obtained results can be introduced by careless alignment between the shaft and indenter tip. Thin films can undergo premature fracture caused non-uniform and misaligned loading. Therefore, prior to each single measurement, the geometry of each sample has to be evaluated and the indenter tip has to be positioned in the middle (center) of each shaft using indenter microscope optics.

In general, MEMS devices as tools to study mechanical properties are relatively simple to fabricate, and measurements are straightforward. However, very thin samples can undergo a failure when loaded with sharp stylus prior the actual measurement. This problem is eliminated when using the tensile method with integrated loading mechanism, and the MEMS SLT test methods. In these methods, loading mechanism and the specimen are fabricated together, and thus the misalignment between them is minimal. The integrated loading structure provides pure tension of the sample avoiding premature fracture. The bulge method also entails characterization of material mechanical properties with no contact loading.

5.2. Young's modulus, residual stress and fracture strength of ALD Al_2O_3, mixed oxide $Al_xTi_yO_z$ and nanolaminated Al_2O_3/TiO_2 thin films

The elastic properties of ALD aluminum oxide depend on the film thickness. Films can withstand large strains without cracking as film thickness reduces. The strain follows a $1/h^2_{Al_2O_3}$ trend, where h is the film thickness [130]. As a function of deposition temperature, elastic properties remain nearly constant when Al_2O_3 is grown at 150–300°C saturating around 170 GPa [69]. However, films become softer when deposited at 110°C (the Young's modulus of ~140 GPa). Elastic properties of free-standing membranes match those measured on supporting substrates (Table 5). Using the bulge and MEMS SLT (Publication **I**), we obtain Young's modulus values 164–165 GPa for Al_2O_3 films deposited at 220°C (±5°C). Nanolaminated and mixed oxide structures have Young's modulus of 148-169 GPa and 151–154 GPa respectively, in reasonable agreement with expected rule-of-mixture law.

Table 5. Young's modulus, residual stress, and fracture strength obtained by bulge and MEMS SLT methods (Publication **I**).

Thin film	MEMS shaft loaded test	Bulge test	MEMS shaft loaded test	Bulge test	MEMS shaft loaded test	Bulge test
	Residual stress (MPa)		Young's Modulus (GPa)		Fracture strength (GPa)	
Al_2O_3	403±18	347±34	164±15	165±21	1.57±0.41	2.56±0.21
$Al_xTi_yO_z$ mixed oxide	389±13	365±23	154±24	151±26	1.17±0.20	2.09±0.17
Al_2O_3/TiO_2 nanolaminate	450±22	450±5	148±37	169±16	1.23±0.14	2.26±0.22

ALD Al_2O_3, mixed oxide $Al_xTi_yO_z$ and nanolaminated Al_2O_3/TiO_2 structures experience tensile stress of hundreds MPa. The bulge and MEMS SLT technique revealed residual stress of 347–403 MPa for Al_2O_3, 365–389 MPa for $Al_xTi_yO_z$, and 450–455 MPa for the nanolaminate (deposited at 220°C). The residual stress level is higher for nanolaminated structures than for Al_2O_3 due to contribution of high residual stress (600–700 MPa for 200°C deposition temperature and 400 MPa for 250°C [131]) of TiO_2. As a function of deposition temperature, the residual stress of Al_2O_3 tends to decrease from 520 MPa at 110°C to 180 MPa at 300°C. As deposition temperature increases films become denser and impurities, e.g., hydrogen, reduce [69]. The tendency is opposite for TiO_2 [67]. The stress increases as a function of temperature. The residual stress is only 133 MPa at 80°C and it increases to 682 MPa at 300 °C due to crystallization of TiO_2 after 200°C.

As typical for ceramic materials, both Al_2O_3 and nanolaminates Al_2O_3/TiO_2 undergo brittle catastrophic fracture during bulge or MEMS SLT testing after pure elastic deformation (Publication **I,** Publication **II**). Nanolaminated or mixed oxide films have lower fracture strength that pure Al_2O_3 films most likely due to low fracture toughness and, therefore, strength of ALD TiO_2 [132]. The reinforcement can be, however, achieved by incorporating a single layer of graphene (Publication **III**). According to the bulge method, membranes of aluminum oxide with graphene layer have higher strain and strength values. The incorporation of CVD graphene layer increases the maximum strain from 0.26% to at least 0.69%. The bulge method revealed that the Al_2O_3-graphene membranes deflects to 23–26 µm at 2 bar, whereas the equally thick reference Al_2O_3 membranes cracks after reaching a deflection of 16–20 µm at fracture pressure of ~0.6 bar. The composite structures remain intact although significant cracking in the Al_2O_3 layer is present. Importantly, the graphene quality also remains high indicating that no graphene damage occurs (no observable shifts of graphene characteristic peaks as measured by Raman spectroscopy). As a function of deposition temperature (Publication **II),** the fracture strength of ALD Al_2O_3 membranes is nearly constant in the range of 2.25–3.00 GPa. The strength of aluminum oxide membranes is comparable with the strength of common MEMS materials such as PECVD silicon carbide, diamond-like carbon, or polysilicon. Their strength is 0.6–1.9 GPa for SiC, 0.7 GPa for diamond-like carbon, and 3.0 GPa for polysilicon [133,134]. LPCVD Si_3N_4 exhibits higher fracture strength values (7 GPa [135]) compared to ALD Al_2O_3-based oxides. However, Si_3N_4 has poor selectivity against SF_6-based plasma etching, therefore membranes only of rectangular shapes can be fabricated by KOH/TMAH etching. Furthermore, LPCVD Si_3N_4 films are typically deposited at temperatures higher than 550°C, which limits their applications on temperature sensitive sublayers or substrates.

ALD thin films, like any other brittle materials, exhibit variation in the reported strength values (Publication **I,** Publication **II**). The source of the variation is perhaps due from the fabrication process: from lithography (some regions might be more/less developed than others which leads to larger/smaller final structures than in the mask design) and from the Bosch process (undercut or notching leads to larger etched structures than initially designed). Due to the fact that the strength is highly dependent on specimen area, therefore, the strength values can be scattered if area even slightly changes from sample to sample.

*Properties of ALD Al_2O_3 thin films after environmental stress (Publication **II**)*

Reliable operation of MEMS devices in a harsh environment remains as an issue. MEMS devices are often subjected to high temperatures or high humidity environments; for example in space automotive or automotive applications. Harsh environment can degrade MEMS performance since mechanical properties change. For example, the resonance frequency of MEMS resonators is highly influenced by environment. If environmental conditions change, stress drifts from tension to compression or vice versa. This leads to the shift of the resonance frequency decreasing MEMS performance [136].

MEMS performance improves by coating the device with only a few nanometers of ALD layer: ALD Al_2O_3 and TiO_2 films are known to increase fatigue lives of silicon and polysilicon MEMS in mild and harsh environments [137-139]. It is therefore essential to characterize the mechanical properties of ALD thin films after environmental stresses.

Environmental effects to mechanical resistance to failure of ALD Al_2O_3 appeared to be strong. The humid environment reduces fracture (Publication **II**) and interfacial strengths [140]. Corrosion reaction most probably causes degradation of a material mechanical performance because cracks initiate and crack-growth rate increases. In the aqueous environment, the surface atoms of a layer react with other species:

$$Al_2O_3 + 3H_2O \rightarrow 2Al(OH)_3 \tag{26}$$

This reaction is in agreement with some reports, which show that Al_2O_3 films convert to hydroxides, i.e. AlO(OH) and $Al(OH)_3$, after immersion to water, especially when films are grown at low-temperatures with high hydrogen content [141]. As a result of the corrosion, cracks initiate at the surface flaws formed during high humidity treatment. Moreover, the ALD Al_2O_3 films are known to dissolve in water-based solutions with an etch rate of 0.2 nm/min [142]. Therefore, the film dissolution can provoke formation of paths for moisture penetration and facilitates strength reduction of aluminum oxide.

Annealing induces strength reduction of Al_2O_3 free-standing films. Many membranes undergo premature failure after annealing, as described in the Publication **II**. The temperature might provoke crack formation due to thermal stress. During the annealing of Al_2O_3, the stress is released with blister formation. The effect is related with both hydrogen and water out-gassing in the film (discussed in the Chapter **4**).

Cyclic loading is known to promote fatigue of materials which leads to microstructural damage and consequently to complete failure. After cyclical loading of ALD Al_2O_3 membranes, no damage was observed. Membrane test structures remained intact after cycling bulge testing. In the Publication **II**, ten cycles with the maximum available ramp rate of >>10 bar/s were applied until 1500 mbar. Next ten cycles with the same ramp rate were applied to the same membrane until 2000 mbar. Most probably, fatigue damage would occur only after higher number of cycles. The mechanical strength of Al_2O_3 films appeared to be, however, dependent on the loading rate (Publication **III**). When the loading rate was fast (100 mbar/s, and total measurement time ~30 s), aluminum oxide could withstand higher loads. In contrast, when the loading was slow (total measurement time > 1 h); aluminum oxide underwent fracture even at lower loads.

6. Adhesion

6. 1. Definition of adhesion

Adhesion is an important material property referred to interfacial capacity to resist mechanical separation. From one point of view, it is defined as energy required to create new free surfaces at the interface of two bonded materials [106,107]. This adhesion is called basic, true, intrinsic or fundamental. The true work of adhesion is evaluated by Young-Dupre equation as follows

$$W_{ad} = \gamma_A + \gamma_B - \gamma_{AB} \quad (27)$$

where γ_A is specific surface free energy of substance *A*, γ_B is the specific surface energy of substance *B* and γ_{AB} is the interfacial energy. W_{ad} depends on type of bonding, and it is determined typically by contact angle measurements in case of liquid coatings (Figure 28) [107].

In case of thermal equilibrium:

$$\gamma_{AB} = \gamma_A - \gamma_B \cos\Theta. \quad (28)$$

The true work adhesion then:

$$W_{ad} = \gamma_B (1 + \cos\Theta), \quad (29)$$

where Θ is the contact angle between the droplet and the substance *A*. The adhesion is based on the change in free energy before and after the contact between the substances *A* and *B*. Therefore, it is possible to quantify the adhesion if substances *A* and *B* are both liquids or one of them is solid and the other liquid.

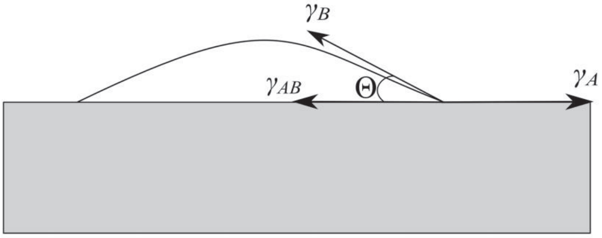

Figure 28. Contact angle measurement: γ_A is specific surface free energy of substance *A, e.g.,* substrate, γ_B is the specific surface energy of substance *B*, *e.g.,* droplet.

In case of thin film, more parameters have to be taken into account to extract true work of adhesion: the types of interaction and the number of interacting units per unit area [143]. In practice, during debonding, film additionally experiences plastic deformation. Therefore, the measured work of adhesion includes also energies dissipated during delamination through plastic deformation:

$$W_{ad,p} = W_{ad} + U_A + U_B + U_{fric}\ , \tag{30}$$

where U_A, U_B, U_{fric} are dissipated plastic energies and energy loss in friction respectively.

Practical or experimental adhesion is defined as interfacial fracture energy Γ or work of fracture per unit area to separate the interface of interest [107]. It can be also determined as force per unit area applied to separate two materials.

The determination of practical adhesion provides information of possible failure between thin films or substrate and thin film. This information is necessary for designing and fabricating reliable and durable MEMS devices which often consist of multiple layers of materials.

6. 2. Methods for determination of adhesion

Adhesion can be characterized using qualitative and quantitative methods. In both approaches, one should take into account such parameters like loading speed and mode (lateral or normal to the interface), mechanical properties of thin film, which can influence the extracted adhesion properties [143]. Quantitative methods estimate energy needed to open up the interface, whereas qualitative methods give just an approximation of the interfacial strength and/or quick comparison adhesion of different thin films [143,144]. Quantitative methods are typically complex. They may have long sample preparation and difficult measurements. However, qualitative methods are often irreproducible. Therefore, quantitative methods are preferred since they provide sufficient information about adhesion energies. The most common quantitative methods include the pull test, the indentation, the scratch test, and the blister test (Figure 29 (a-d)).

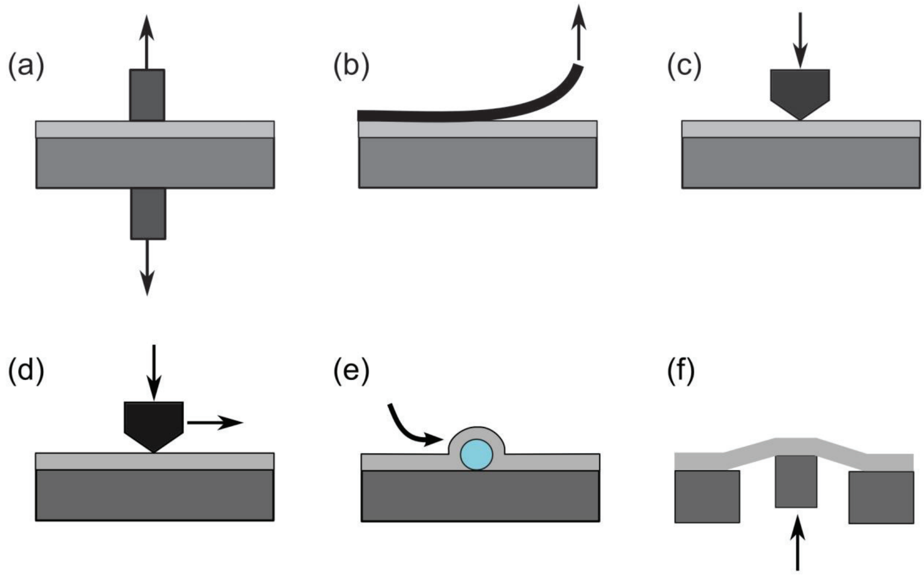

Figure 29. Methods to determine adhesion: (a) pull test; (b) tape peel test; (c) indentation; (d) scratch test; (e) lateral displacement adhesion testing; (f) MEMS SLBT.

Pull test

In the pull test, a pin attached to the back of the film is pulled in the perpendicular direction. Another possible configuration (Figure 29 (a)) of the test is when two symmetric pins are attached to the film (from the front side) and to the substrate (from the back side). Then the pins are pulled off against each other with the same force. As a result of the test, adhesion properties can be extracted as a function of force F needed to delaminate the coating.

The main advantage of the technique is that it can be applied for both brittle and ductile thin films. In addition, the sample preparation is simple and straightforward. The main disadvantage is that the interpretation of data is complex due to a wide scatter in results. Non-uniform thickness, any changes in sample preparation, pin misalignment can lead to considerably variable data and difficulties in interpretation of locus of failure (surfaces involved in bond failure). Failure can take place at the interface (adhesive failure) and/or in the film/substrate material (cohesive failure). Typically pins are attached with an epoxy or adhesive, which can penetrate to the coating. Therefore, the measurement of adhesion and further interpretation of results can be challenging and even spurious [106,144].

Tape peel test

The peel test (Figure 29 (b)) is the easiest, the fastest, and the most inexpensive test. It is an effective method which provides, however, only qualitative information about adhesion. It consists of a tape applied to the coating. This tape is subsequently peeled off. If film delaminates with the tape, then the adhesion is unacceptable and vice versa. The method is suitable mainly for soft, thick and weakly bonded coatings on a rigid substrate. In addition, the tape/film bond interface should be stronger than the film/substrate interface [106].

Indentation

In the indentation test (Figure 29 (c)), an indenter tip pierces the coating under controllable conditions. As a result, the film compresses and then delaminates. The load-depth curves are used to extract adhesion properties. Therefore, qualitative and quantitative data is extracted. However, when the coating is very thin or hard, then it can undergo failure before the actual delamination (Figure 30). Under high compression, substrate and coating can both be cracked. It renders the interpretation of the locus of failure uncertain. A great advantage of indentation technique is that commercial equipment is readily available. Furthermore, no special sample preparation is needed [144].

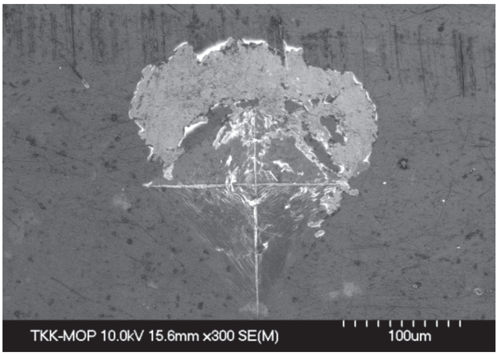

Figure 30. Failure of diamond-like carbon coating from titanium substrate during indentation debonding test (SEM courtesy Jussi Lyytinen).

Scratch test

The scratch method (Figure 29(d)) is an extension of the indentation technique, where the indenter stylus slides across the film to initiate the delamination. The load gradually increases until the film is completely removed resulting in a scratch channel. The adhesion strength is evaluated as a function of critical load when the scratch channel started forming [106,144]. One can assess the adhesion qualitatively, if mechanical properties are determined from the same film.

The critical load when coating starts to delaminate can be calculated as [107]

$$F^* = \frac{\pi {d_c}^2}{8}\left(\frac{2EW_{ad,p}}{h}\right)^{1/2}, \qquad (31)$$

where h is film thickness, d_c is the width of the scratch at the critical load, E is the Young's modulus of the film.

The main disadvantage is that direct contact between film and indenter promotes deformation of the substrate, film and therefore the analysis and interpretation of data are challenging. The method is well-suited to study adhesion of hard brittle coatings. But the method is limited for soft coatings due to formation of mounds at the edge of the scratch track.

New lateral displacement adhesion testing

Lateral displacement adhesion testing (Figure 29 (e)) or the interfacial mechanical testing of adhesion with embedded microspheres into the coating is created as the extension of scratch technique or when scratch method is not applicable (Publication **V**). During the scratch method very thin films fracture along with underlying substrate, because film adheres tenaciously to the substrate.

The mechanical testing with embedded microspheres is applied to evaluate adhesion between thin films (<100 nm) and substrate. The incorporation of microspheres into the coating facilitates detachment of the coating. The adhesion is evaluated as the ratio of applied lateral force F to the delaminated area A.

Resultant detached areas are then observed under scanning electron microscope along with energy dispersive X-ray spectroscopy and with image analysis software. This is important because as majority of tests with the laterally applied force, this method leads to cohesive cracking. Careful investigation of the delaminated and peeled area gives information of the adhesion between extra thin films and various substrates (Figure 31).

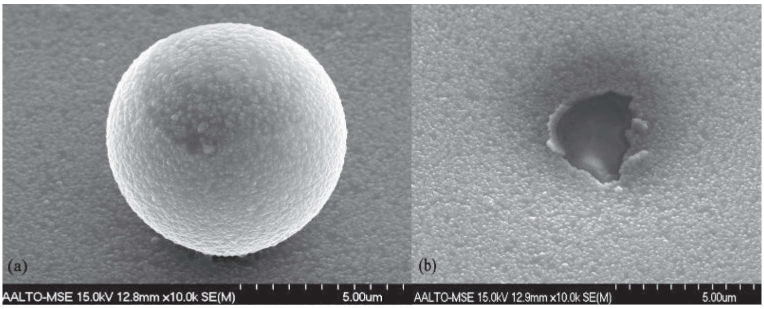

Figure 31. SEM image of the (a) embedded SiO_2 sphere into ALD TiO_2 coating on glass substrate before the measurement (b) delaminated area after the measurement (Publication **V**).

This method offers several advantages: thin films can be either brittle or ductile; the substrate and spheres can be of any material. The sample preparation is easy, and the loading set-up can be commercially available. The microscopes can be fitted within the set-up to ease the examination of the adhesion properties. Furthermore, any deformation of the substrate is avoided. Thus even very thin films can be studied without substrate influence.

The incorporated SiO_2 spheres into the ALD TiO_2 coating facilitated its delamination from the substrate (Publication **V**). The new test method provided quantitative and qualitative comparison of adhesion of ALD films on glass substrate. We distinguished several groups of possible interfacial failure. In the first group, the delamination occurs at film-substrate interface. In the second group, the interfacial failure occurs between film and sphere. The third group is mixed between first and second groups: when delamination occurs at both film/substrate and film/sphere interfaces. The average critical detaching force of 100-nm-thick TiO_2 (deposited at 200°C) from the glass substrate is 0.38±0.11 mN and corresponding interfacial failure stress is 36±12 MPa. As it has been shown in our recent work [145], this method is suitable to evaluate adhesion between ALD TiO_2 or Al_2O_3 and silicon substrate. The detachment of TiO_2 from silicon substrate is achieved with the critical load of 0.18 mN and reaching similar stress values of 31.6±3.8 MPa as in the case with glass substrate. In general, the critical load (for 100 and 300 nm thick films) decreases as the deposition temperature of TiO_2 increases. Similar trend is observed for 300-nm-thick aluminum oxide films.

MEMS shaft-loaded blister testing (SLBT)

MEMS SLBT (Figure 29 (f)) is a relatively simple method for qualitative and quantitative assessment of adhesion between different films located on a substrate. The test structure consists of suspended annular membrane with an axisymmetric shaft which mechanically loads the membrane (Figure 32 (0,1)) to promote the delamination. When threshold point is reached, then the delamination starts (Figure 32 (1)). The threshold point is observed as a change in the slope of displacement curve behavior as the output of microindentation measurement. The delamination proceeds further with increasing the load to a preset value (Figure 32 (3)), which is held for some time, and then followed by gradual unloading.

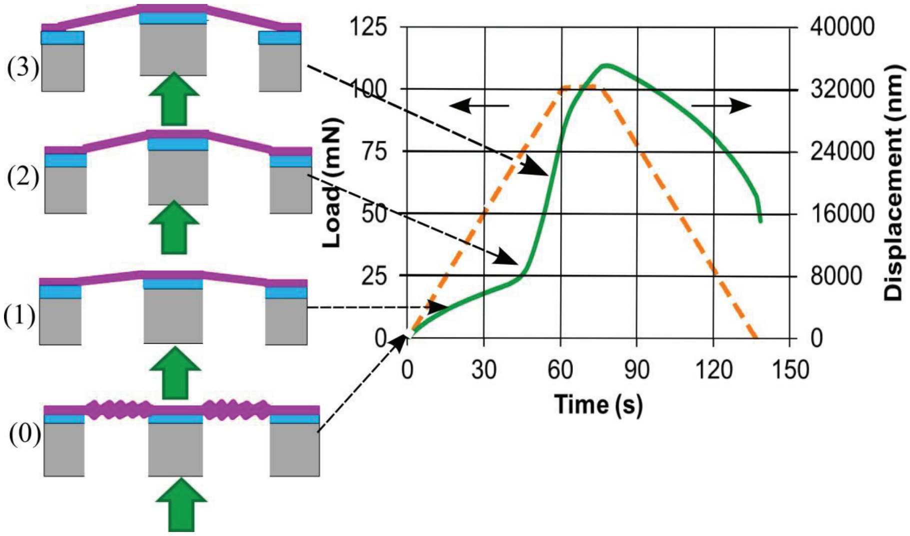

Figure 32. MEMS SLBT methodology: (0) the indenter approaches the shaft surface; (1)shaft loading;(2)critical load when the delamination starts, (3) delamination continues as the shaft is loaded (Publication **IV**).

The method can be modified with only one film on substrate to evaluate adhesion between substrate and coating of interest. A single measurement can give also information about the mechanical properties such as Young's modulus, residual stress and fracture strength.

The work of adhesion is assessed as energy released in debonded area [146,147], and defined as

$$W_{ad,p} = \left(\frac{1}{16\pi^4 Eh}\right)^{1/3}\left(\frac{F}{a_2}\right)^{4/3}, \qquad (32)$$

where a_2 is radius of the blister (Figure 33 (a)), and the central point load F versus central deflection w is given by Equation (24).

An alternative approach to measure work of adhesion is the consideration of the energy dissipated per unit area upon extending a crack along the interface, or

$$W_{ad,p} = \frac{W_d}{A_{del}} \tag{33}$$

where the delaminated area A_{del} is determined by $A_{del} = \pi\left(a_2^2 - (a + a_1)^2\right)$, and the energy dissipation W_d is defined as the hysteresis area from loading and unloading curves (Figure 33) or $W_{pl} = \int_0^1 \mathrm{Fdl} + \int_1^2 \mathrm{Fdl} - \int_2^3 \mathrm{Fdl}$.

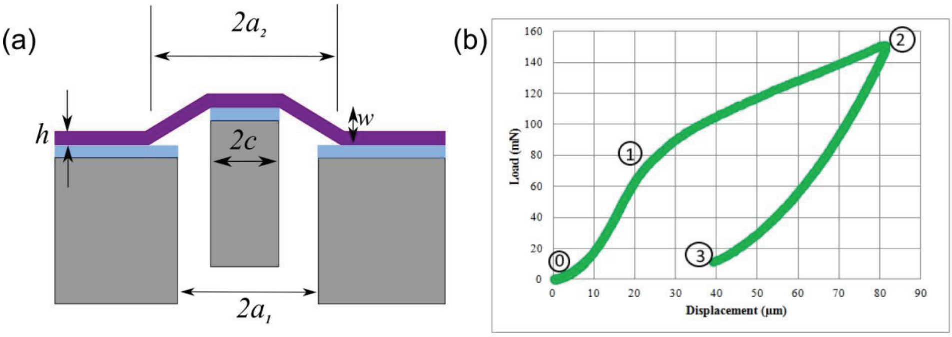

Figure 33. (a) Cross-sectional view of MEMS SLBT; (b) load-displacement curve obtained from the MEMS SLBT measurement 0-1-2-3 refers to the same stages as in Figure 32 (Publication **IV**).

Adhesion between sputtered thin films (platinum, copper and copper with chromium adhesion layer) and ALD aluminum oxide was measured by MEMS SLBT technique (Publication **IV**). The test structures were examined by applying the load along the microshaft using CSM Microindenter. The microindenter load induced displacement which then caused the delamination between thin films and therefore, contributed to obtain the work of adhesion. Comparing copper and copper with underlying chromium layer, the delamination of the film with adhesive layer start at higher displacement and load values, proving the adhesive action of chromium. The adhesion values are corresponding of 1.4 J/m² for Cu/Al_2O_3 system and 1.75 J/m² for Cu/Cr/Al_2O_3 (evaluated by Equation (32) and (33)). Platinum films have the lowest adhesion to Al_2O_3 of 1.15–1.16 J/m². The adhesion energies between ALD Al_2O_3 and sputtered films are higher (indicating that adhesion is stronger) than of typical adhesion values between bulk Al_2O_3 and sputtered copper and platinum films. The work of adhesion is typically in the range of 0.3–0.7 J/m² [148,149] for the bulk aluminum oxide and sputtered films. The difference can be due to different bonding mechanisms for bulk material and thin film and for two thin film materials.

Comparison of the methods to evaluate adhesion

Each method has a number of advantages and disadvantages. Many of them can be nearly ideal. The ideal test to assess adhesion should have the following properties [106,144]:

- Adhesion between the two materials must be weaker than cohesion of each material;
- No dependence of the size and shape of the material samples;
- Quantitative simplicity and clarity;
- Reproducible and not very time consuming
- Ease of specimen preparation.

In general, each method is good for the certain purpose. Table 6 summarizes the main advantages and disadvantages of each technique. If it is necessary to have an easy estimation of adhesion strength, then tape peel test is the best candidate. However, reproducibility concerns arise. Simple sample preparation methods such as indentation and scratch method give reproducible qualitative and quantitative data, but the interpretation of results can be challenging. Moreover, in both methods indenter is in a direct contact with the coating. The indenter can damage the underlying substrate, and therefore qualitative analysis becomes complex and results ambiguous. The embedding of microspheres allows overcoming of these drawbacks. In this method, microspheres with the coating are easily detached with no influence of the substrate. As a result, qualitative and quantitative data of adhesion can be extracted for a variety of films/substrate systems. MEMS SLBT is very stable, and reproducible method. Mechanical properties including adhesion, Young’s modulus and residual stress are the output of a single measurement. It is very advantageous method for qualitative and quantitative assessment of adhesion between thin films or thin film and substrate systems.

Table 6. Main advantages and disadvantages of mechanical testing of adhesion.

Method	**Advantage**	**Disadvantage**
Tape peel [144]	Easy sample preparation	Only for soft, flexible coatings on rigid
	Control of the delamination rate	Qualitative only
	Straightforward	Reproducibility concerns
Pull [144]	Easy sample preparation	Alignment
	A wide variety of coating/substrate	Bonding of adhesive or solder
	Both qualitative and quantitative	Uncontrollable failure mode
Indentation [144]	Easy sample preparation	Difficult quantitative analysis
	A wide variety of coating/substrate systems	Thin film in a direct contact with an indenter
	Commercial instruments readily	Destructive
Scratch [106]	Easy sample preparation	Mainly for hard coatings
	Commercial instruments readily	Destructive
	Both qualitative and quantitative	Thin film in a direct contact with an indenter
Embedded microspheres (Publication **V**)	Easy sample preparation	Difficult quantitative analysis
	A wide variety of coating/substrate	Destructive
	Commercial instruments readily	Finding the spheres
MEMS SLBT (Publication **IV**)	Fully quantitative and qualitative	Relatively long sample preparation
	Variety of the size and shape of the material	Highly adhering coatings break before delamination
	No contact to the film itself	
	Reproducible	
	Adhesion between two thin films	
	Control of the delamination rate	
	Non-destructive	
	Clearly interfacial separation (adhesive failure)	

7. Summary and conclusions

This thesis presents the recent results obtained by the author on mechanical properties of ALD films. The thesis concentrates on Young's modulus, residual stress, fracture and interfacial strength. The knowledge of these parameters is important for designing novel MEMS devices and for assuring reliable performance of MEMS devices manufactured from these materials.

In this thesis, the basic principles of various deposition methods and structure-process-stress relationship are described. The thesis contains an overview of fabrication techniques used to manufacture MEMS test structures as tools to study mechanical properties of various thin films. Different MEMS devices used to characterize mechanical properties are discussed and compared. Similarly, methods to analyze adhesion properties of thin films are overviewed and juxtaposed.

Standard bulge technique (Publications **I**, **II, III, IV**) was used to evaluate the mechanical properties of ALD-based thin films. In this method, the overpressure is smoothly and uniformly applied along the membrane diameter to yield information about fracture, elastic properties and residual stress of suspended thin films. The method was accomplished with SWLI allowing nanometer-scale z-resolution of film deflection and true shape of the deflected membranes over millimeter areas.

Novel MEMS structures were developed and successfully applied to obtain mechanical properties of ALD films. The developed methods open new possibilities for mechanical assessments also of other thin films.

In the MEMS SLT technique (Publications **I**, **IV**), the test structure consists of suspended annular membrane with an axisymmetric shaft, which deflects the membrane. From the analysis of force-displacement behavior, mechanical properties of thin films can be calculated. The MEMS SLT is attractive for precise mechanical characterization because shaft has no contact to the film. This configuration avoids premature fracture induced by the indenter. The data presents true value of thin film properties because there is no influence of underlying substrate. Data interpretation and analysis is clear and straightforward. Our test chip contains nine microshafts of the same size. Therefore one can easily obtain statistical data from a single chip. Using microindentation, the measurements can be done automatically by presetting the actual loading position (the center of each shaft), force and approach speed. This eases the measurements and efforts. The method provides excellent repeatability: the load-deflection responses from microshafts of the same sizes are identical. Moreover, microindentation results in thousands of data points from a single measurement allowing fitting with a high accuracy.

MEMS SLT can be further employed to characterize adhesion properties between two thin films (Publication **IV**). The method provides repeatable and simultaneously quantitative and qualitative measurements of adhesion between thin films. The structure is suitable to study adhesion properties of various thin films or between thin film/substrate systems of choice.

In case of strong adhesion of the film to the substrate, the debonding events can be problematic: thin films tend to break before the actual delamination. Therefore, it is important to develop new methods to overcome these issues. Publication **V** deals with characterization of adhesion properties on a planar glass substrate of very thin ALD TiO_2 layers, which typically adhere tenaciously to the substrate. The embedding of silica nanospheres facilitates delamination of the film and, therefore, extraction of lateral critical failure stress. Importantly, the sample preparation is simple and quantitative data can be easily obtained. In the future, we plan to evaluate the adhesion properties of other substrate-sphere-thin film systems.

The obtained results on mechanical properties of ALD films are promising for applying these materials in membrane-based MEMS devices. ALD films are flexible, with no excessive residual stress, and high fracture strength. ALD films studied in this doctoral dissertation had residual tensile stress in the range of 350–450 MPa, the Young's modulus of 150–170 GPa, and the fracture strength of 1.17 GPa–3.00 GPa. Tensile stress in this range is beneficial to obtain flatness of free-standing structures. The Young's modulus of this range shows that ALD films are elastic and flexible. The fracture strength is significant, especially because membranes can have large free-standing area being very thin at the same time. In the future, it will be interesting to investigate film thickness-strength correlation (size effect) of free-standing membranes. It was recently shown that ALD Al_2O_3 films exhibit higher strength when thickness is reduced: 5.5 GPa fracture strength for thicknesses below 50 nm and 3.5 GPa for 100-nm-thick film (measured with microarchitected 3D-printed cellular materials) [150]. We observed similar tendency: 3 GPa for 75 nm-thick membranes and 1.57 GPa for 200-nm-thick (Publication **I, II**). Nevertheless, it will be worthwhile to explore thinner membranes. Bulge and MEMS shaft-loaded methods developed in this thesis are good candidates for these studies. Furthermore, the mechanical properties of very thin ALD films might be influenced by substrate on which they are grown. Therefore, an additional investigation of possible substrate-induced changes of mechanical properties should be performed.

High humidity and annealing at high temperatures is found, however, to reduce resistance to failure of Al_2O_3 membranes even by 50%. In case of humidity, corrosion and dissolution in aqueous environment seem to be the reasons of strength decrease. The thesis contains additional results on ALD Al_2O_3 behavior upon annealing as the investigation of the reasons fracture reduction after annealing. According to TOF-ERDA measurements, annealing greatly promote diffusion of water and hydrogen from the film, while carbon and aluminum concentrations undergo no significant changes. Hydrogen and water out-diffusion provoke the blistering formation, which probably lead to the strength reduction. However, more experimental work is needed to understand the failure of ALD Al_2O_3 films after environmental stress.

Comparing nanolaminates Al_2O_3/TiO_2 or mixed oxide $Al_xTi_yO_z$ with single-layer Al_2O_3, nanolaminates have lower fracture strength, comparable elastic properties, and slightly higher residual stress than Al_2O_3. The mechanical properties of nanolaminates follow expected rule-of-mixture law.

Incorporation of a single graphene layer between two ALD Al_2O_3 films, as described in Publication **III**, can greatly improve the resistance to failure of ALD aluminum oxide membranes by a factor of minimum three. This composite structure appeared to be more crack-resistant without reducing the quality of graphene. The next step is to develop and to build ALD graphene/Al_2O_3 membrane-based MEMS devices for sensing applications.

Appendix

1. Weibull analysis

The scatter in the fracture strength of brittle materials is significant because the failure starts from the small flaws, which are scattered in the material. Fracture can initiate from the largest surface or volumetric imperfections, and it can vary from sample to sample. Furthermore, the fracture strength reduces with increasing the actual sample area as probability of finding defects increases. Therefore, the strength of brittle materials needs to be defined with a probability function. The most suitable model for characterization of probability of fracture of brittle materials is the probabilistic Weibull distribution. The Weibull formula is based on weakest link model, which states that if the weakest link fails under applied load, the entire structure fails. This is valid for brittle materials when the failure undergoes catastrophically and rapidly.

If the probability of failure is $P_f(\sigma)$ under applied stress σ, therefore the probability of survival or reliability is $1\text{-}P_f$. If the specimen consists of N identical elements (links), subjected to the same stress, therefore the failure probability is the same for every element. In this case, the survival probability of the entire structure will depend on the probability of failure of each element [151]

$$P_s = 1 - P_{f,structure} = (1 - P_f)^N . \tag{1}$$

Taking logarithm from both sides and assuming that the failure probability of every element is small ($ln\,(1\text{-}P_f) \approx \text{-}P_f$) gives

$$\ln(1 - P_{f,structure}) = -NP_f . \tag{2}$$

The probability of structure failure can be written then

$$P_{f,structure}(\sigma) = 1 - \exp[-NP_f(\sigma)]. \tag{3}$$

A continuous specimen consists of discrete elements N, which can be defined as the ratio of the total volume V to the volume of the element of material V_o (unit volume), whose probability of fracture is postulated by Weibull as $P_{f;V}(\sigma) = (\sigma\text{-}\sigma_o/\sigma_c)^m$, where σ_o is the threshold stress, below which no failure can occur (set to zero for brittle materials), σ_c is the characteristic failure strength value of a material volume $V{=}V_o$ or when $P_{f,structure} = (1 - e^{-1}) \cdot 100\% = 63\%$ and m is the Weibull modulus, which is related to the scatter of the strength data and depends on distribution of flaw sizes in the specimen.

Thus the failure probability for a specimen under uniformly applied stress σ is described by Weibull function [150-153]

$$P_f = 1 - \exp\left[-\frac{V}{V_0} \left(\frac{\sigma}{\sigma_c} \right)^m \right], \tag{4}$$

or since $V=V_o$

$$P_f = 1 - \exp\left[-\left(\frac{\sigma}{\sigma_c} \right)^m \right]. \tag{5}$$

Figure 1 represents an example of the Weibull distribution: failure probability (%) versus fracture strength (GPa), obtained after the bulge fracture measurement for 75-nm-thick ALD aluminum oxide-based free-standing membranes.

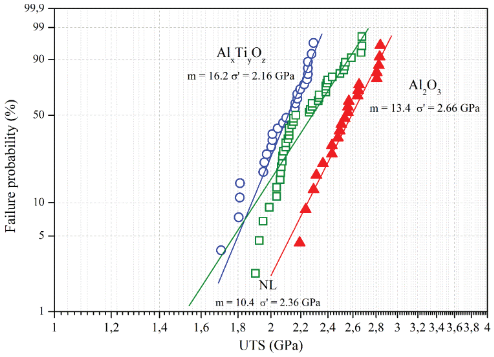

Figure 1. Weibull diagram for ALD Al_2O_3, mixed oxide $Al_xTi_yO_z$ and nanolaminated Al_2O_3/TiO_2 75 nm-thick membranes, obtained after the bulge testing (Publication **I**). σ' refers to the characteristic strength. UTS is the ultimate tensile stress or fracture strength.

Often times, the strength is characterized by the average value and standard deviation, defined as:

$$\bar{\sigma} = \frac{\sigma_c}{(V/V_0)^{1/m}} \cdot \Gamma(1+\frac{1}{m}), \tag{6}$$

$$s = \sqrt{\bar{\sigma}^2 \cdot \left(\frac{\Gamma(1+\frac{2}{m})}{\Gamma^2(1+\frac{1}{m})} \right)}, \tag{7}$$

where $\Gamma(z)$ is the gamma function.

Commonly the Weibull formula (Equation (4)) is expressed by taking natural logarithm of probability of survival *(1-P_f)* twice to extract Weibull modulus from the slope as follows

$$\ln\left[\ln(\frac{1}{1-P_f}) \right] = m\ln(\sigma) - [m\ln(\sigma_0) - \ln(V/V_0)]. \tag{8}$$

References

[1]. Nguyen, N. T., Huang, X., & Chuan, T. K. (2002). MEMS-micropumps: a review. *Journal of fluids Engineering*, 124(2), 384-392.

[2]. Sainiemi, L, Grigoras K, & Franssila S. Suspended nanostructured alumina membranes. *Nanotechnology* 20.7 (2009): 075306.

[3]. Shoji, S., Nakagawa, S., & Esashi, M. (1990). Micropump and sample-injector for integrated chemical analyzing systems. *Sensors and Actuators A: Physical*, 21(1), 189-192.

[4]. Olsson, A., Stemme, G., & Stemme, E. (1995). A valve-less planar fluid pump with two pump chambers. *Sensors and Actuators A: Physical*, 47(1), 549-556.

[5]. Briand, D., Colin, S., Gangadharaiah, A., Vela, E., Dubois, P., Thiery, L., & De Rooij, N. F. (2006). Micro-hotplates on polyimide for sensors and actuators. *Sensors and Actuators A: Physical,* 132(1), 317-324.

[6]. Mahalik, Nitaigour Premchand, (2008) *MEMS*. Tata McGraw-Hill Education.

[7]. Ying, X., Luo, J., Wang, P., Cui, M., Zhao, Y., Li, G., & Zhu, P. (2003). Ultra-thin freestanding diamond window for soft X-ray optics. *Diamond and related materials*, 12(3), 719-722.

[8]. Torma, P. T., Sipila, H. J., Mattila, M., Kostamo, P., Kostamo, J., Kostamo, E., Lipsanen, H., Nelms, N., Shortt, B., Bavdaz, M., & Laubis, C. (2013). Ultra-thin silicon nitride X-ray windows. *IEEE Transactions on Nuclear Science,* 60(2), 1311-1314.

[9]. Grigoras, K., Franssila, S., & Airaksinen, V. M. (2008). Investigation of sub-nm ALD aluminum oxide films by plasma assisted etch-through. *Thin Solid Films*, 516(16), 5551-5556.

[10]. Norrman, S., Andersson, T., Granqvist, C. G., & Hunderi, O. (1978). Optical properties of discontinuous gold films. *Physical Review B*, 18(2), 674.

[11]. Wasa, K. (Ed.). (2012). *Handbook of Sputter Deposition Technology: Fundamentals and Applications for Functional Thin Films, Nano-materials and MEMS*. William Andrew.

[12]. Franssila, S. (2010) *Introduction to Microfabrication*. John Wiley & Sons.

[13]. McConnell, A. D., Uma, S., & Goodson, K. E. (2001). Thermal conductivity of doped polysilicon layers. *Journal of Microelectromechanical Systems,* 10(3), 360-369.

[14]. Huang, Q. A., & Lee, N. K. S. (1999). Analysis and design of polysilicon thermal flexure actuator. *Journal of Micromechanics and Microengineering*, 9(1), 64.

[15]. Cordill, M. J., Bahr, D. F., Moody, N. R., & Gerberich, W. W. (2007). Adhesion measurements using telephone cord buckles. *Materials Science and Engineering: A*, 443(1), 150-155.

[16]. Vinci, R. P., & Vlassak, J. J. (1996). Mechanical behavior of thin films. *Annual Review of Materials Science*, 26(1), 431-462.

[17]. Berdova M., Brandt M, Grönberg L., Sillanpää M & Franssila S, (2013) Implementation of ALD thin films as stress compensation layers in NEMS, Topical Conference on Atomic Layer deposition, ALD AVS 2013.

[18]. Costescu, R. M., Cahill, D. G., Fabreguette, F. H., Sechrist, Z. A., & George, S. M. (2004). Ultra-low thermal conductivity in W/Al_2O_3 nanolaminates. *Science*, 303(5660), 989-990.

[19]. Moharrami, N., & Bull, S. J. (2014). A comparison of nanoindentation pile-up in bulk materials and thin films. *Thin Solid Films*, 572, 189-199.

[20]. Petrov, I., Barna, P. B., Hultman, L., & Greene, J. E. (2003). Microstructural evolution during film growth. *Journal of Vacuum Science & Technology A*, 21(5), S117-S128.

[21]. Thompson, C. V., & Carel, R. (1996). Stress and grain growth in thin films. *Journal of the Mechanics and Physics of Solids*, 44(5), 657-673.

[22]. Hoffman, D. W., McCune, R. C., Rossnagel, S. M., Cuomo, J. J., & Westwood, W. D. (1990). Microstructural control of plasma-sputtered refractory coatings. Handbook of Plasma Processing Technology, 483-517.

[23]. Buschow, K. J., Cahn, R. W., Flemings, M. C., Ilschner, B., Kramer, E. J., & Mahajan, S. (2001). *Encyclopedia of materials*. Science and technology, 1, 11.

[24]. Tipek, A., Ripka, P., Hulicius, E., Hospodková, A., & Neužil, P. New Technologies and Materials. *Modern Sensors Handbook*, 477-511.

[25]. Leplan, H., Robic, J. Y., & Pauleau, Y. (1996). Kinetics of residual stress evolution in evaporated silicon dioxide films exposed to room air. *Journal of Applied Physics*, 79(9), 6926-6931.

[26]. Leplan, H., Geenen, B., Robic, J. Y., & Pauleau, Y. (1995). Residual stresses in evaporated silicon dioxide thin films: Correlation with deposition parameters and aging behavior. *Journal of Applied Physics*, 78(2), 962-968.

[27]. Windischmann, H. (1991). Intrinsic stress in sputtered thin films. *Journal of Vacuum Science & Technology A*, 9(4), 2431-2436.

[28]. Hoffman, R. W., Daniels, R. D., & Crittenden, E. C. (1954). The cause of stress in evaporated metal films. *Proceedings of the Physical Society. Section B*, 67(6), 497.

[29]. Kelly, P. J., & Arnell, R. D. (2000). Magnetron sputtering: a review of recent developments and applications. *Vacuum*, 56(3), 159-172.

[30]. Alfonso, E., Olaya, J., & Cubillos, G. (2012). Thin film growth through sputtering technique and its applications. *Crystallization–Science and Technology*, InTech, Croatia, 397-432.

[31]. Mahieu, S., Ghekiere, P., Depla, D., & De Gryse, R. (2006). Biaxial alignment in sputter deposited thin films. *Thin Solid Films*, 515(4), 1229-1249.

[32]. Freund, L. B., & Suresh, S. (2004). Thin film materials: stress, defect formation and surface evolution. Cambridge University Press.

[33]. Ohring, M. (2001). *Materials science of thin films*. Academic press.

[34]. Hinze, J., & Ellmer, K. (2000). In situ measurement of mechanical stress in polycrystalline zinc-oxide thin films prepared by magnetron sputtering. *Journal of Applied Physics*, 88(5), 2443-2450.

[35]. Hoffman, D. W., & Thornton, J. A. (1977). Internal stresses in sputtered chromium. *Thin Solid Films*, 40, 355-363.

[36]. Janssen, G. C. A. M., & Kamminga, J. D. (2004). Stress in hard metal films. *Applied Physics Letters*, 85(15), 3086-3088.

[37]. Iosad, N. N., Jackson, B. D., Polyakov, S. N., Dmitriev, P. N., & Klapwijk, T. M. (2001). Reactive magnetron sputter-deposition of NbN and (Nb, Ti)N films related to sputtering source characterization and optimization. *Journal of Vacuum Science & Technology A*, 19(4), 1840-1845.

[38]. Sandu, C. S., Benkahoul, M., Parlinska-Wojtan, M., Sanjinés, R., & Lévy, F. (2006). Morphological, structural and mechanical properties of NbN thin films deposited by reactive magnetron sputtering. *Surface and Coatings Technology*, 200(22), 6544-6548.

[39]. Hultman, L. (2000). Thermal stability of nitride thin films. *Vacuum*, 57(1), 1-30.

[40]. Wahl, G., Davies, P. B., Bunshah, R. F., Joyce, B. A., Bain, C. D., Wegner, G., Remmers, M., Walsh, F. C., Hieber, K., Sundgren, J.-E., Bachmann, P. K., Miyazawa, S., Thelen, A., Strathmann, H. and Edler, K. J. 2014. *Thin Films*. Ullmann's Encyclopedia of Industrial Chemistry. 1–75.

[41]. Hess, W. T. (1995). Kirk-Othmer encyclopedia of chemical technology. John Wiley & Sons Ltd., New York.

[42]. Pierson, H. O. (1999). *Handbook of chemical vapor deposition: principles, technology and applications*. William Andrew.

[43]. Temple-Boyer, P., Rossi, C., Saint-Etienne, E., & Scheid, E. (1998). Residual stress in low pressure chemical vapor deposition SiNx films deposited from silane and ammonia. *Journal of Vacuum Science & Technology A*, 16(4), 2003-2007.

[44]. Koutsoureli, M., Tavassolian, N., Papaioannou, G., & Papapolymerou, J. (2011). Dielectric charging in capacitive microelectromechanical system switches with silicon nitride. *Applied Physics Letters*, 98(9), 093505.

[45]. Choy, K. L. (2003). Chemical vapour deposition of coatings. *Progress In Materials Science*, 48(2), 57-170.

[46]. Martin, P. M. (2009). *Handbook of deposition technologies for films and coatings: science, applications and technology*. William Andrew.

[47]. Winchester, K. J., & Dell, J. M. (2001). Tunable Fabry-Pérot cavities fabricated from PECVD silicon nitride employing zinc sulphide as the sacrificial layer. *Journal of Micromechanics and Microengineering*, 11(5), 589.

[48]. Martyniuk, M., Antoszewski, J., Musca, C. A., Dell, J. M., & Faraone, L. (2007). Dielectric thin films for MEMS-based optical sensors. *Microelectronics Reliability*, 47(4), 733-738.

[49]. Claassen, W. A. P., Valkenburg, W. G. J. N., Willemsen, M. F. C., & vd Wijgert, W. M. (1985). Influence of deposition temperature, gas pressure, gas phase composition, and RF frequency on composition and mechanical stress of plasma silicon nitride layers. *Journal of the Electrochemical Society*, 132(4), 893-898.

[50]. Obraztsov, A. N. (2009). Chemical vapour deposition: making graphene on a large scale. *Nature Nanotechnology*, 4(4), 212-213.

[51]. Riikonen, J., Kim, W., Li, C., Svensk, O., Arpiainen, S., Kainlauri, M., & Lipsanen, H. (2013). Photo-thermal chemical vapor deposition of graphene on copper. *Carbon*, 62, 43-50.

[52]. Zhang, Y., Zhang, L., & Zhou, C. (2013). Review of chemical vapor deposition of graphene and related applications. *Accounts of Chemical Research*, 46(10), 2329-2339.

[53]. Nair, R. R., Blake, P., Grigorenko, A. N., Novoselov, K. S., Booth, T. J., Stauber, T., Peres, N. M. R., & Geim, A. K. (2008). Fine structure constant defines visual transparency of graphene. *Science*, 320(5881), 1308-1308.

[54]. Stankovich, S., Dikin, D. A., Dommett, G. H., Kohlhaas, K. M., Zimney, E. J., Stach, E. A., Piner, R.D., Nguyen, S. T., & Ruoff, R. S. (2006). Graphene-based composite materials. *Nature*, 442(7100), 282-286.

[55]. Gong, L., Young, R. J., Kinloch, I. A., Riaz, I., Jalil, R., & Novoselov, K. S. (2012). Optimizing the reinforcement of polymer-based nanocomposites by graphene. *ACS Nano*, 6(3), 2086-2095.

[56]. George, S. M. (2009). Atomic layer deposition: an overview. *Chemical Reviews*, 110(1), 111-131.

[57]. Puurunen, R. L. (2005). Surface chemistry of atomic layer deposition: A case study for the trimethylaluminum/water process. *Journal of Applied Physics*, 97(12), 121301.

[58]. Leskelä, M., & Ritala, M. (2003). Atomic layer deposition chemistry: recent developments and future challenges. *Angewandte Chemie International Edition*, 42(45), 5548-5554.

[59]. King, J. S., Heineman, D., Graugnard, E., & Summers, C. J. (2005). Atomic layer deposition in porous structures: 3D photonic crystals. *Applied Surface Science*, 244(1), 511-516.

[60]. Elam, J. W., Routkevitch, D., Mardilovich, P. P., & George, S. M. (2003). Conformal coating on ultrahigh-aspect-ratio nanopores of anodic alumina by atomic layer deposition. *Chemistry of Materials*, 15(18), 3507-3517.

[61]. Groner, M. D., Fabreguette, F. H., Elam, J. W., & George, S. M. (2004). Low-temperature Al_2O_3 atomic layer deposition. *Chemistry of Materials*, 16(4), 639-645.

[62]. Niinistö, J., Mäntymäki, M., Kukli, K., Costelle, L., Puukilainen, E., Ritala, M., & Leskelä, M. (2010). Growth and phase stabilization of HfO_2 thin films by ALD using novel precursors. *Journal of Crystal Growth*, *312*(2), 245-249.

[63]. Lim, J., & Lee, C. (2007). Effects of substrate temperature on the microstructure and photoluminescence properties of ZnO thin films prepared by atomic layer deposition. *Thin Solid Films*, 515(7), 3335-3338.

[64]. Goldstein, D. N., McCormick, J. A., & George, S. M. (2008). Al_2O_3 atomic layer deposition with trimethylaluminum and ozone studied by in situ transmission FTIR spectroscopy and quadrupole mass spectrometry. *The Journal of Physical Chemistry C*, 112(49), 19530-19539.

[65]. Ott, A. W., Klaus, J. W., Johnson, J. M., & George, S. M. (1997). Al_3O_3 thin film growth on Si (100) using binary reaction sequence chemistry. *Thin Solid Films*, 292(1), 135-144.

[66]. Cameron, M. A., Gartland, I. P., Smith, J. A., Diaz, S. F., & George, S. M. (2000). Atomic layer deposition of SiO_2 and TiO_2 in alumina tubular membranes: pore reduction and effect of surface species on gas transport. *Langmuir*, 16(19), 7435-7444.

[67]. Huang, Y., Pandraud, G., & Sarro, P. M. (2013). Characterization of low temperature deposited atomic layer deposition TiO_2 for MEMS applications. *Journal of Vacuum Science & Technology A*, 31(1), 01A148.

[68]. Puurunen, R. L., Saarilahti, J., & Kattelus, H. (2007). Implementing ALD layers in MEMS processing. ECS Transactions, 11(7), 3-14.

[69]. Ylivaara, O. M., Liu, X., Kilpi, L., Lyytinen, J., Schneider, D., Laitinen, M., Julin, J., Ali, S., Sintonen, S., Berdova, M., Haimi, E., Sajavaara, T., Ronkainen, H., Lipsanen, H., Koskinen, J., Hannula, S-P., & Puurunen, R. L. (2014). Aluminum oxide from trimethylaluminum and water by atomic layer deposition: The temperature dependence of residual stress, elastic modulus, hardness and adhesion. *Thin Solid Films*, 552, 124-135

[70]. Miikkulainen, V., Leskelä, M., Ritala, M., & Puurunen, R. L. (2013). Crystallinity of inorganic films grown by atomic layer deposition: Overview and general trends. *Journal of Applied Physics*, 113(2), 021301.

[71]. Puurunen, R. L., Sajavaara, T., Santala, E., Miikkulainen, V., Saukkonen, T., Laitinen, M., & Leskelä, M. (2011). Controlling the crystallinity and roughness of atomic layer deposited titanium dioxide films. *Journal of Nanoscience and Nanotechnology*, 11(9), 8101-8107.

[72]. Leskelä, M., Kemell, M., Kukli, K., Pore, V., Santala, E., Ritala, M., & Lu, J. (2007). Exploitation of atomic layer deposition for nanostructured materials. *Materials Science and Engineering: C*, 27(5), 1504-1508.

[73]. Meyer, J., Schmidt, H., Kowalsky, W., Riedl, T., & Kahn, A. (2010). The origin of low water vapor transmission rates through Al_2O_3/ZrO_2 nanolaminate gas-diffusion barriers grown by atomic layer deposition. *Applied Physics Letters*, 96(24), 243308-243308.

[74]. Tallarida, M., Weisheit, M., Kolanek, K., Michling, M., Engelmann, H. J., & Schmeisser, D. (2011). Atomic layer deposition of nanolaminate oxide films on Si. *Journal of Nanoparticle Research*, 13(11), 5975-5983.

[75]. Michler, G. H. (2008). *Electron microscopy of polymers*. Springer.

[76]. Sintonen, S., Ali, S., Ylivaara, O. M., Puurunen, R. L., & Lipsanen, H. (2014). X-ray reflectivity characterization of atomic layer deposition Al_2O_3/TiO_2 nanolaminates with ultrathin bilayers. *Journal of Vacuum Science & Technology A*, 32(1), 01A111.

[77]. Hanhijarvi, K., Kassamakov, I., Aaltonen, J., Heikkinen, V., Sainiemi, L., Franssila, S., & Haeggstrom, E. (2013). Through-silicon stroboscopic characterization of an oscillating MEMS thermal actuator using supercontinuum interferometry. *IEEE/ASME Transactions on Mechatronics*, 18(4), 1418-1420.

[78]. Putkonen, M., Sajavaara, T., Niinistö, L., & Keinonen, J. (2005). Analysis of ALD-processed thin films by ion-beam techniques. *Analytical and bioanalytical chemistry*, 382(8), 1791-1799.

[79]. Spearing, S. M. (2000). Materials issues in microelectromechanical systems (MEMS). *Acta Materialia*, 48(1), 179-196.

[80]. Triyoso, D. H., Hegde, R. I., Grant, J., Fejes, P., Liu, R., Roan, D, Ramon, M., Werho, D., Rai, R., La, L.B., Baker, J., Garza, C., Guenther, T., White Jr., B. E., and & Tobin, P. J. (2004). Film properties of ALD HfO_2 and La_2O_3 gate dielectrics grown on Si with various pre-deposition treatments. *Journal of Vacuum Science & Technology B: Microelectronics and Nanometer Structures*, 22(4), 2121-2127.

[81]. Arnold, C. B., & Piqué, A. (2007). Laser direct-write processing. *MRS bulletin*, 32(01), 9-15.

[82]. Häfner, M., Pruss, C., & Osten, W. (2011). Laser direct writing. *Optik & Photonik*, 6(4), 40-43.

[83]. Berdova, M., Cho, S. U., Pirkkalainen, J. M., Sulkko, J., Song, X., Hakonen, P. J., & Sillanpää, M. A. (2013). Micromanipulation transfer of membrane resonators for circuit optomechanics. *Journal of Micromechanics and Microengineering*, 23(12), 125024.

[84]. Sainiemi, L. (2009). Cryogenic deep reactive ion etching of silicon micro and nanostructures, TKK dissertation.

[85]. Jansen, H., Gardeniers, H., de Boer, M., Elwenspoek, M., & Fluitman, J. (1996). A survey on the reactive ion etching of silicon in microtechnology. *Journal of Micromechanics and Microengineering*, 6(1), 14.

[86]. Laermer, F., Franssila, S., Sainiemi, L., & Kolari, K. (2010). *Deep reactive ion etching*. Handbook of silicon based MEMS materials and technologies, 349-374.

[87]. Sökmen, Ü., Stranz, A., Fündling, S., Wehmann, H. H., Bandalo, V., Bora, A., Tornow, M., Waag, A., & Peiner, E. (2009). Capabilities of ICP-RIE cryogenic dry etching of silicon: review of exemplary microstructures. *Journal of Micromechanics and Microengineering*, 19(10), 105005.

[88]. Kuribayashi, H., Hiruta, R., Shimizu, R., Sudoh, K., & Iwasaki, H. (2003). Shape transformation of silicon trenches during hydrogen annealing. *Journal of Vacuum Science & Technology A*, 21(4), 1279-1283.

[89]. Chen, K. S., Ayón, A., & Spearing, S. M. (2000). Controlling and testing the fracture strength of silicon on the mesoscale. *Journal of the American Ceramic Society*, 83(6), 1476-1484.

[90]. Chen, K. S., Ayón, A. A., Zhang, X., & Spearing, S. M. (2002). Effect of process parameters on the surface morphology and mechanical performance of silicon structures after deep reactive ion etching (DRIE). *Journal of Microelectromechanical Systems*, 11(3), 264-275.

[91]. Kiihamäki, J., & Franssila, S. (1999). Pattern shape effects and artefacts in deep silicon etching. *Journal of Vacuum Science & Technology A*, 17(4), 2280-2285.

[92]. Lai, S. L., Johnson, D., & Westerman, R. (2006). Aspect ratio dependent etching lag reduction in deep silicon etch processes. *Journal of Vacuum Science & Technology A*, 24(4), 1283-1288.

[93]. Henry, M. D., Walavalkar, S., Homyk, A., & Scherer, A. (2009). Alumina etch masks for fabrication of high-aspect-ratio silicon micropillars and nanopillars. *Nanotechnology*, 20(25), 255305.

[94]. Sainiemi, L., & Franssila, S. (2007). Mask material effects in cryogenic deep reactive ion etching. *Journal of Vacuum Science & Technology B*, 25(3), 801-807.

[95]. Grigoras, K., Sainiemi, L., Tiilikainen, J., Säynätjoki, A., Airaksinen, V. M., & Franssila, S. (2007). Application of ultra-thin aluminum oxide etch mask made by atomic layer deposition technique. In *Journal of Physics: Conference Series*, 61(1), 369-373.

[96]. Dekker, J., Kolari, K., & Puurunen, R. L. (2006). Inductively coupled plasma etching of amorphous Al_2O_3 and TiO_2 mask layers grown by atomic layer deposition. *Journal of Vacuum Science & Technology B: Microelectronics and Nanometer Structures*, 24(5), 2350-2355.

[97]. Wang, L., Travis, J. J., Cavanagh, A. S., Liu, X., Koenig, S. P., Huang, P. Y., George S. M., & Bunch, J. S. (2012). Ultrathin oxide films by atomic layer deposition on graphene. *Nano letters*, 12(7), 3706-3710.

[98]. Belyansky, M. (2012). Thin-Film Strain Engineering and Pattern Effects in Dielectrics CVD. *Handbook of Thin Film Deposition*, 89.

[99]. Miller, D. C., Herrmann, C. F., Maier, H. J., George, S. M., Stoldt, C. R., & Gall, K. (2007). Thermo-mechanical evolution of multilayer thin films: Part I. Mechanical behavior of Au/Cr/Si microcantilevers. *Thin Solid Films*, 515(6), 3208-3223

[100]. Miller, D. C., Herrmann, C. F., Maier, H. J., George, S. M., Stoldt, C. R., & Gall, K. (2007). Thermo-mechanical evolution of multilayer thin films: Part II. Microstructure evolution in Au/Cr/Si microcantilevers. *Thin Solid Films*, 515(6), 3224-3240.

[101]. Schmidt, J., Merkle, A., Brendel, R., Hoex, B., Van de Sanden, M. C. M., & Kessels, W. M. M. (2008). Surface passivation of high-efficiency silicon solar cells by atomic-layer-deposited Al_2O_3. Progress in photovoltaics: research and applications.

[102]. Hennen, L., Granneman, E. H. A., & Kessels, W. M. M. (2012, June). Analysis of blister formation in spatial ALD Al_2O_3 for silicon surface passivation. In Photovoltaic Specialists Conference (PVSC), 2012 38th IEEE (pp. 001049-001054).

[103]. Bordihn, S. (2014). Surface Passivation by Al2O3-based Film Stacks for Si Solar Cells, Doctoral dissertation, Technische Universiteit Eindhoven.

[104]. Vermang, B., Goverde, H., Uruena, A., Lorenz, A., Cornagliotti, E., Rothschild, A., John, J., Poortmans, J., & Mertens, R. (2012). Blistering in ALD Al_2O_3 passivation layers as rear contacting for local Al BSF Si solar cells. *Solar Energy Materials and Solar Cells*, 101, 204-209.

[105]. Berdova, M., Rontu, V., Sajavaara, T., Eskelinen, A. P., & Franssila, S. (2014) Blistering effect of ALD Al_2O_3 grown with trimethylaluminum and water. In Baltic ALD.

[106]. Mittal, K. L. (1976). Adhesion aspects of metallization of organic polymer surfaces. *Journal of Vacuum Science and Technology*, 13(1), 19-25.

[107]. Volinsky, A. A., Moody, N. R., & Gerberich, W. W. (2002). Interfacial toughness measurements for thin films on substrates. *Acta Materialia*, 50(3), 441-466.

[108]. Gad-el-Hak, M. (Ed.). (2001). *The MEMS handbook*. CRC press.

[109]. Zhang, T. Y., Su, Y. J., Qian, C. F., Zhao, M. H., & Chen, L. Q. (2000). Microbridge testing of silicon nitride thin films deposited on silicon wafers. *Acta Materialia*, 48(11), 2843-2857.

[110]. Liimatainen, V., Venalainen J., Koverola, M., Zhou, Q., Lyytinen, J., Koskinen, J., Rontu, V., Berdova, M., & Franssila, S. (2014) Characterization of nano-coated micro-and nanostructures by pushing. In International Conference on Manipulation, Manufacturing and Measurement on the Nanoscale (3M-NANO).

[111]. Osterberg, P. M., & Senturia, S. D. (1997). M-TEST: a test chip for MEMS material property measurement using electrostatically actuated test structures. *Journal of Microelectromechanical Systems,* 6(2), 107-118.

[112]. Baek, C. W., Kim, Y. K., Ahn, Y., & Kim, Y. H. (2005). Measurement of the mechanical properties of electroplated gold thin films using micromachined beam structures. *Sensors and Actuators A: Physical*, 117(1), 17-27.

[113]. Cardinale, G. F., Howitt, D. G., McCarty, K. F., Medlin, D. L., Mirkarimi, P. B., & Moody, N. R. (1996). Analysis of residual stress in cubic boron nitride thin films using micromachined cantilever beams. *Diamond and Related Materials*, 5(11), 1295-1302.

[114]. Walmsley, B. A., Liu, Y., Hu, X. Z., Bush, M. B., Winchester, K. J., Martyniuk, M., Dell, J. M., & Faraone, L. (2005). Effects of deposition temperature on the mechanical and physical properties of silicon nitride thin films. *Journal of Applied Physics*, 98(4), 044904.

[115]. Koskinen, J., Steinwall, J. E., Soave, R., & Johnson, H. H. (1993). Microtensile testing of free-standing polysilicon fibers of various grain sizes. *Journal of Micromechanics and Microengineering*, 3(1), 13.

[116]. Sharpe Jr, W. N., Bagdahn, J., Jackson, K., & Coles, G. (2003). Tensile testing of MEMS materials - recent progress. *Journal of Materials Science,* 38(20), 4075-4079.

[117]. Buchheit, T. E., Glass, S. J., Sullivan, J. R., Mani, S. S., Lavan, D. A., Friedmann, T. A., & Janek, R. (2003). Micromechanical testing of MEMS materials. *Journal of Materials Science*, *38*(20), 4081-4086.

[118]. Greek, S., Ericson, F., Johansson, S., & Schweitz, J. Å. (1997). In situ tensile strength measurement and Weibull analysis of thick film and thin film micromachined polysilicon structures. *Thin Solid Films*, 292(1), 247-254.

[119]. Sharpe Jr, W. N., Turner, K. T., & Edwards, R. L. (1999). Tensile testing of polysilicon. *Experimental Mechanics*, 39(3), 162-170.

[120]. Yoshioka, T., Ando, T., Shikida, M., & Sato, K. (2000). Tensile testing of SiO_2 and Si_3N_4 films carried out on a silicon chip. *Sensors and Actuators A: Physical*, 82(1), 291-296.

[121]. Mitchell, J. S., Zorman, C. A., Kicher, T., Roy, S., & Mehregany, M. (2003). Examination of bulge test for determining residual stress, Young's modulus, and Poisson's ratio of 3C-SiC thin films. *Journal of Aerospace Engineering*, 16(2), 46-54.

[122]. Hohlfelder, R. J. (1999). Bulge and blister testing of thin films and their interfaces.

[123]. Beams, J. W. (1959). Mechanical properties of thin films of gold and silver. *Structure and properties of thin films*, 183-192.

[124]. Vlassak, J. J., & Nix, W. D. (1992). A new bulge test technique for the determination of Young's modulus and Poisson's ratio of thin films. *Journal of Materials Research*, 7(12), 3242-3249.

[125]. Pan, J. Y., Lin, P., Maseeh, F., & Senturia, S. D. (1990). Verification of FEM analysis of load-deflection methods for measuring mechanical properties of thin films. In Solid-State Sensor and Actuator Workshop.

[126]. Tabata, O., Kawahata, K., Sugiyama, S., & Igarashi, I. (1989). Mechanical property measurements of thin films using load-deflection of composite rectangular membrane. In *Micro Electro Mechanical Systems, Proceedings, an Investigation of Micro Structures, Sensors, Actuators, Machines and Robots*.

[127]. Maier-Schneider, D., Maibach, J., & Obermeier, E. (1995). A new analytical solution for the load-deflection of square membranes. *Journal of Microelectromechanical Systems,* 4(4), 238-241.

[128]. Pickhardt, V. Y., & Smith, D. L. (1977). Fabrication of high-strength unsupported metal membranes. *Journal of Vacuum Science and Technology*, 14(3), 823-825.

[129]. Wan, K. T., & Dillard, D. A. (2003). Adhesion of a flat punch adhered to a thin pre-stressed membrane. *The Journal of Adhesion*, 79(2), 123-140.

[130]. Jen, S. H., Bertrand, J. A., & George, S. M. (2011). Critical tensile and compressive strains for cracking of Al_2O_3 films grown by atomic layer deposition. *Journal of Applied Physics*, 109(8), 084305.

[131]. Puurunen, R. L., Saarilahti, J., & Kattelus, H. (2007). Implementing ALD layers in MEMS processing. *ECS Transactions*, 11(7), 3-14.

[132]. Zhang, L., Prosser, J. H., Feng, G., & Lee, D. (2012). Mechanical properties of atomic layer deposition-reinforced nanoparticle thin films. *Nanoscal*e, 4(20), 6543-6552.

[133]. Sharpe Jr, W. N., Bagdahn, J., Jackson, K., & Coles, G. (2003). Tensile testing of MEMS materials—recent progress. Journal of Materials Science, 38(20), 4075-4079.

[134]. Espinosa, H. D., Prorok, B. C., Peng, B., Kim, K. H., Moldovan, N., Auciello, O., Carlisle, J. A., Gruen, D. M., & Mancini, D. C. (2003). Mechanical properties of ultrananocrystalline diamond thin films relevant to MEMS/NEMS devices. *Experimental Mechanics*, 43(3), 256-268.

[135]. Koskinen, J., & Johnson, H. H. (1988, January). Silicon nitride fibers using micro fabrication methods. In *MRS Proceedings*, 130(63).

[136]. Kazinczi, R., Mollinger, J. R., & Bossche, A. (2002). Environment-induced failure modes of thin film resonators. *Journal of Micro/Nanolithography, MEMS, and MOEMS*, 1(1), 63-69.

[137]. Baumert, E. K., Theillet, P. O., & Pierron, O. N. (2011). Fatigue-resistant silicon films coated with nanoscale alumina layers. *Scripta Materialia*, 65(7), 596-599.

[138]. Budnitzki, M., & Pierron, O. (2009). The influence of nanoscale atomic-layer-deposited alumina coating on the fatigue behavior of polycrystalline silicon thin films. *Applied Physics Letters*, 94(14), 141906.

[139]. Sadeghi-Tohidi, F., Samet, D., Graham, S., & Pierron, O. N. (2014). Comparison of the cohesive and delamination fatigue properties of atomic-layer-deposited alumina and titania ultrathin protective coatings deposited at 200° C. *Science and Technology of Advanced Materials,* 15(1), 015003.

[140]. Ou, K. S., Lin, I., Wu, P. H., Huang, Z. K., Chen, K. S., & Zhang, X. (2009). Mechanical Characterization of Atomic Layer Deposited (ALD) Alumina for Applications in Corrosive Environments. In *MRS Proceedings*, 1222.

[141]. Carcia, P. F., McLean, R. S., Li, Z. G., Reilly, M. H., & Marshall, W. J. (2012). Permeability and corrosion in ZrO_2/Al_2O_3 nanolaminate and Al2O3 thin films grown by atomic layer deposition on polymers. *Journal of Vacuum Science & Technology A*, 30(4), 041515.

[142]. Puurunen, R. L., Kiihamäki J., & Kattelus, H. (2005) Controlling the solubility of ALD aluminium oxide in deionised water, In *AVS Topical Conference on Atomic Layer Deposition.*

[143]. Mittall, K. L. (1995). Adhesion measurement of films and coatings: A commentary. *Adhesion Measurement of Films and Coatings*, 1-13.

[144]. Lacombe R. *Adhesion measurement methods, Theory and Practice*. CRC, Press, New York, 2006

[145]. Lyytinen, J., Berdova, M., Hirvonen, P., Liu, X. W., Franssila, S., Zhou, Q., & Koskinen, J. (2014). Interfacial mechanical testing of atomic layer deposited TiO_2 and Al_2O_3 on a silicon substrate by the use of embedded SiO_2 microspheres. *RSC Advances*, 4(70), 37320-37328.

[146]. Wan, K. T., Di Prima, A., Ye, L., & Mai, Y. W. (1996). Adhesion of nylon-6 on surface treated aluminium substrates. *Journal of Materials Science*, 31(8), 2109-2116.

[147]. Na, H., Chen, P., Wan, K. T., Wong, S. C., Li, Q., & Ma, Z. (2012). Measurement of adhesion work of electrospun polymer membrane by shaft-loaded blister test. *Langmuir*, 28(16), 6677-6683.

[148]. Venkataraman, S. K., Nelson, J. C., Hsieh, A. J., Kohlstedt, D. L., & Gerberich, W. W. (1993). Continuous microscratch measurements of thin film adhesion strengths. *Journal of Adhesion Science and Technology*, 7(12), 1279-1292.

[149]. Ward, T. R., Alemany, P., & Hoffmann, R. (1993). Adhesion of rhodium, palladium, and platinum to alumina and the reduction of nitric oxide on the resulting surfaces: a theoretical analysis. *The Journal of Physical Chemistry*, 97(29), 7691-7699

[150]. Bauer, J., Schroer, A., Schwaiger, R., Tesari, I., Lange, C., Valdevit, L., & Kraft, O. (2015). Push-to-pull tensile testing of ultra-strong nanoscale ceramic–polymer composites made by additive manufacturing. *Extreme Mechanics Letters*, 3, 105-112.

[151]. Jones, P. T., Johnson, G. C., & Howe, R. T. (1999). Statistical characterization of fracture of brittle MEMS materials. In Symposium on Micromachining and Microfabrication. International Society for Optics and Photonics.

[152]. Lu, C., Danzer, R., & Fischer, F. D. (2002). Fracture statistics of brittle materials: Weibull or normal distribution. *Physical Review E*, 65(6), 067102.

[153]. Kapels, H., Aigner, R., & Binder, J. (2000). Fracture strength and fatigue of polysilicon determined by a novel thermal actuator. IEEE Transactions on Electron Devices, 47(7), 1522-1528.

Aalto-DD 119/2015

9 789526 063447

ISBN 978-952-60-6344-7 (printed)
ISBN 978-952-60-6345-4 (pdf)
ISSN-L 1799-4934
ISSN 1799-4934 (printed)
ISSN 1799-4942 (pdf)

Aalto University
School of Chemical Technology
Department of Materials Science and Engineering
www.aalto.fi